Materials Today Bio 14 (2022) 100288

Contents lists available at ScienceDirect

Materials Today Bio

journal homepage: www.journals.elsevier.com/materials-today-bio

Cascade-activatable NO release based on GSH-detonated "nanobomb" for multi-pathways cancer therapy

Yi Feng [a], Hanxi Zhang [a], Xiaoxue Xie [a], Yu Chen [a], Geng Yang [a], Xiaodan Wei [a], Ningxi Li [a], Mengyue Li [a], Tingting Li [a], Xiang Qin [a], Shun Li [a], Fengming You [b], Chunhui Wu [a], Hong Yang [a,**], Yiyao Liu [a,b,*]

[a] Department of Biophysics, School of Life Science and Technology, University of Electronic Science and Technology of China, Chengdu, 610054, Sichuan, PR China
[b] TCM Regulating Metabolic Diseases Key Laboratory of Sichuan Province, Hospital of Chengdu University of Traditional Chinese Medicine, No. 39 Shi-er-qiao Road, Chengdu, 610072, Sichuan, PR China

ARTICLE INFO

Keywords:
Reduction-responsive biodegradation
Gas therapy
Photodynamic therapy
Tumor hypoxia relief
Tumor microenvironment reversal

ABSTRACT

Therapeutic approaches of combining conventional photodynamic therapy (PDT) with other adjuvant treatments to sensitize PDT represent an appealing strategy. Herein, a novel synergetic "nanobomb" strategy based on glutathione (GSH)-responsive biodegradation was proposed to effectively destroy tumors expeditiously and accurately. This "nanobomb" was rationally constructed via the simultaneous encapsulation of methylene blue (MB) and L-arginine (L-Arg) into polyethylene glycol (PEG) modified mesoporous organosilicon nanoparticles (MON). The resulting L-Arg/MB@MP initially exhibited prolonged blood circulation, improved bioavailability, and enhanced tumor accumulation in mice after tail vein injection according to the pharmacokinetic investigations, before the nanoparticles were entirely excreted. Under laser irradiation, L-Arg/MB@MP produced remarkable reactive oxygen species (ROS) directly for PDT therapy, while a portion of ROS may oxidize L-Arg to generate nitric oxide (NO) not only for gas therapy (GT) but also serve as a biological messenger to regulate vasodilation to alleviate the tumor hypoxia. Subsequently, the rapidly released NO was further oxidized to reactive nitrogen species, which together with ROS promote immunogenic cell death by inducing G2/M cell-cycle arrest and apoptosis in cancer cells, and eventually resulting in enhanced anti-tumor immune responses. Moreover, the GSH depletion in tumor tissues induced by L-Arg/MB@MP biodegradation can cooperate with GT to amplify the therapeutic effect of PDT. These results demonstrate that this "nanobomb" provides new ideas for clinical translation to treat tumor patients in terms of synergistic PDT-GT nanotherapy in hypoxic-solid tumors.

1. Introduction

Photodynamic therapy (PDT) has long been considered one of the most minimally invasive and potentially utilized therapeutic approaches in the fight against cancer-based on the irreversible damage to cancer cells caused by highly reactive oxygen species (ROS) generated from photosensitizers activated by laser exposure [1–3]. While the clinical application of PDT in cancer therapy is seriously restricted by the insufficient oxygen supply in tumor regions [4], consumption of ROS by intracellular high concentrations of glutathione (GSH) [5], and the unsatisfactory accumulation of photosensitizers at the tumor site by the weakened enhanced permeability and retention (EPR) effect or lacking targeting [5–7]. In particular, hypoxia (low oxygen) has been described as one of the crucial factors that cause tumor angiogenesis and metastasis in solid tumors finally cause PDT resistance [8–11]. Unfortunately, conventional PDT may worsen the hypoxic conditions, rendering tumor cells less susceptible to ROS-induced death [12]. Furthermore, aggravation of tumor hypoxia during PDT will also promote tumor cells to escape additional factors associated with therapy, resulting in severer resistance, and decreased therapeutic potentials [13]. Moreover, hypoxia-induced immune suppression of tumor microenvironment (TME) can contribute to tumor cells escape from immune surveillance and ultimately facilitate tumor growth, development, and metastasis [14]. Thus, clinical techniques that improve the sensitivity of hypoxic tumor cells to PDT and

* Corresponding author. Department of Biophysics, School of Life Science and Technology, University of Electronic Science and Technology of China, Chengdu, 610054, Sichuan, PR China.
** Corresponding author.
E-mail addresses: yanghongyh@uestc.edu.cn (H. Yang), liuyiyao@uestc.edu.cn (Y. Liu).

https://doi.org/10.1016/j.mtbio.2022.100288
Received 22 March 2022; Received in revised form 9 May 2022; Accepted 10 May 2022
Available online 13 May 2022

reverse or alleviate the hypoxic TME in solid tumors are critical for achieving the optimal therapeutic efficacy of PDT.

Recently, gas therapy (GT) utilizing gaseous transmitters based on nitric oxide (NO) has emerged as a "green" and novel therapy with negligible side effects for the alleviation of hypoxia in TME to further sensitize oxygen-consuming treatments [15–19]. NO as an endogenous messenger molecule plays a regulative role in numerous pathological and physiological processes, including neural activity [20], cardiovascular homeostasis [21], angiogenesis [22], and immune response to infection [21]. Therefore, been encouraged by the excellent versatile functions of NO, many researchers have paid significant efforts to investigate the potential therapeutic applications of NO, particularly in the field of cancer therapy. It has been documented those high concentrations of NO (>1 μM) can not only remarkably inhibit the growth of tumors [15], but can also enhance the efficacy of chemotherapy by overcoming multi-drug resistance [23], also cooperatively the PDT [16], radiotherapy [24], or photothermal therapy [25]. More importantly, NO-mediated vasodilation will increase blood perfusion then efficiently relieve tumor-associated hypoxia [23,26]. Moreover, NO can react with ROS to yield more harmful reactive nitrogen oxides (RNS), such as peroxynitrite ($ONOO^-$) molecules, which can exacerbate DNA breakage and trigger apoptosis, finally enhanced the therapeutic impact of ROS on cancer cells [15,16,20]. While low concentrations of NO, on the other hand, are expected to have a positive influence on tumor development and metastasis [27]. Additionally, since the gaseous NO showed an extremely short half-life, highly sensitive reactivity, and poor tumor tissues accumulation [28], it seems especially essential to achieve the precise control of NO release in spatial, temporal, and dose for on-demand GT.

Herein, to address these challenges, biodegradable disulfide-bridged mesoporous organosilicon nanoparticles (MON) as drug delivery systems were introduced to realize controlled release of ROS and NO. In comparison with traditional inorganic mesoporous silica, direct incorporation of disulfide bond (-S-S-) into the framework of MON can specifically respond to the reducing microenvironment intracellularly or within the tumor tissue realizing GSH-responsive biodegradation of nanocarriers [29–32]. Simultaneously, the consumption of intracellular GSH by nanoparticles would further alleviate the strong reducing environment in tumor cells, which will be beneficial for the production of ROS and amplify the PDT therapeutic effects [33,34]. Taking the above points into account, in this work, we engineered a PEG-coated MON to co-delivery photosensitizer (methylene blue, MB) and NO donors (L-arginine, L-Arg) for synergistic PDT-GT cancer therapy (Scheme 1). As expected, the L-Arg/MB@MP nanoplatform exhibited a high blood-circulation half-life and excellent tumor accumulation *in vivo*. Once L-Arg/MB@MP was accumulated into the reductive TME with a high concentration of GSH properties, the -S-S- in the framework of MP will break up in response to the reductive TME. The subsequent structure collapse process was analogous to the detonation of a "nanobomb", which MB and L-Arg loaded inside the bombs rapidly releasing from the nanoparticles and transforming into therapeutic gas to perform its anti-tumor function. Meanwhile, the fragments of the bombs formed by biological degradation were mainly excreted via the renal system or gastrointestinal route. In addition, ROS-triggered NO generation that aimed to alleviate hypoxia at the tumor site via vasodilatation, thereby down-regulating both HIF-1α and PD-L1 expression to reverse the immunosuppressive TME. On the other hand, the combined PDT-GT markedly enhanced dendritic cells (DCs)-mediated phagocytosis of cells dying (an immunogenic cell death (ICD) induced by abundant ROS and RNS), and finally increase the activation of cytotoxic T cells. Significantly, cytotoxicity of L-Arg/MB@MP achieved through a synergistic action of GT and PDT indicates an RNS-sensitization mechanism that enables it possible to amplify the therapeutic effects of PDT. Therefore, this "nanobomb" is a promising nanoplatform that integrates alleviating hypoxia and reversing the immunosuppressive TME to achieve effective anti-tumor treatment by PDT-GT.

2. Materials and methods

2.1. Materials and reagents

Bis(triethoxysilylpropyl) disulfide (BTES), Cetyltrimethylammonium chloride (CTAC), triethanolamine (TEA), N-hydroxysuccinimide (NHS, >97.0%), Tetraethylorthosilicate (TEOS), N-(3-Dimethylaminopropyl)-N′-ethylcarbodiimide hydrochloride (EDC, >98.0%), 2′,7′-dichlorofluorescein-diacetate (DCFH-DA), and 3-aminopropyltriethoxysilane (APTES) were obtained from Sigma-Aldrich (MO, USA). MB was obtained from shanghai Yuanye Bio-Technology Co., Ltd., (Shanghai, China). 4′,6-diamidino-2-phenylindole dihydrochloride (DAPI), RPMI 1640 cell culture medium, antibodies against Cdc25c, p-Cdc25c, and fetal bovine serum (FBS) were taken from Gibco (Thermo Fisher Scientific, Waltham, MA, USA). Singlet oxygen sensor green (SOSG), propidium iodide (PI), calcein-AM, JC-1 probe, the cell counting kit (CCK-8), Annexin V-fluorescein isothiocyanate (FITC)/PI staining kit, Adenosine triphosphate (ATP) assay kit, antibodies against PD-L1, and lysosome staining kit were obtained from the Beyotime Institute of Biotechnology (Shanghai, China). L-Arginine and vitamin C (V_C) were purchased from Aladdin-Reagent Co. Ltd. (China). Antibodies against Cdc2 (#28439), p-Cdc2 (#4539), Cyclin B (#4135), Caspase-3 (#14220), cleaved caspase-3 (#9664), Bcl-2 (#3498), Bax (#2772), p53 (#2524), and HIF-1α (#36169) were bought from Cell Signaling Technology (USA). Deionized water was used in all other experiments except for preparing simulated body fluid (SBF). All the mentioned chemicals and reagents were used directly without further purification.

2.2. Preparation of mesoporous organosilica nanoparticles (MON), surface PEGylated MON (MP), and dual drug-loaded nanoparticles (L-Arg/MB@MP)

The MON were synthesized using a soft-templating methodology [32]. Briefly, CTAC (2 g), TEA (0.08 g), and deionized water (20 mL) were mixed with uniformity at 95 °C for 1 h. Then TEOS (1 mL) and BTES (0.2 mL) were mixed adequately under ultrasound conditions and subsequently added dropwise into the above-mixed liquid with continuous stirring at 95 °C for 4 h. Finally, the centrifugally collected mesoporous organosilicon nanoparticles (MON) were extracted by stirring in a solution of sodium chloride (NaCl) in methanol (8 mg/mL, 48 h) for three rounds at 40 °C to remove the surfactants CTAC. The aminated nanoparticles (MON-NH_2) were synthesized by a classical method using APTES [33].

To covalently modify a PEG layer onto the surface of MON-NH_2, the PEGylation process was conducted via an amide reaction. Firstly, the carboxyl group of PEG_{5000} (HOOC–CH_2–O-(CH_2CH_2O-)$_n$$CH_2$-COOH) was activated by the addition of NHS and EDC in the Dimethyl sulfoxide (DMSO) solution at room temperature. Then, the MON-NH_2 nanoparticles suspension was added to the above solution and the reaction mixture was continuously stirred at room temperature for 48 h. Finally, the surface PEGylated MON (denoted as MP) was collected through a 5 kDa molecular ultrafiltration tube.

For the preparation of the L-Arg/MB@MP, MON-NH_2 (40 mg) was dispersed into 10 mL of ultrapure water containing 200 mg of L-Arg stirred at room temperature. After stirring for 24 h, the L-Arg loaded particles (named as L-Arg@MON) were collected by centrifugation. Then the L-Arg@MON was added into the PEG_{5000} (2 mg/mL) solution mixed with NHS and EDC under ultrasonication and then stirred for another 24 h. Furthermore, the PEGylated L-Arg@MON (denoted as L-Arg@MP) was washed several times and further purified through dialysis. Finally, the L-Arg@MP (40 mg) was dispersed in 20 mL ultrapure water containing MB (1 mg/mL) and stirred for 24 h. Finally, the resulting L-Arg/MB@MP was obtained by centrifugation and dried via vacuum freeze-drying for further use. Free MB was also loaded into MP to formed MB@MP according to the same synthesis process of L-Arg@MP.

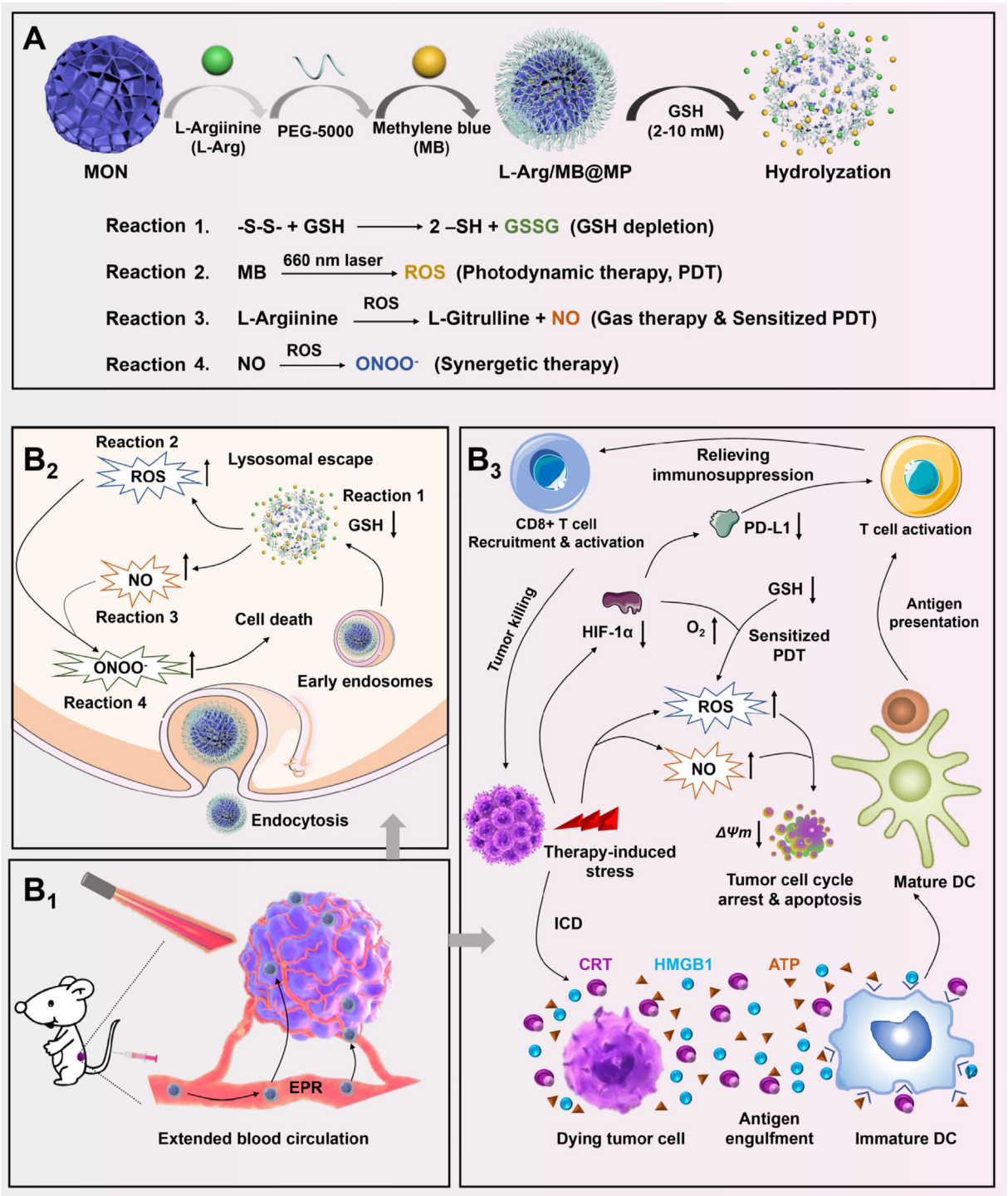

Scheme 1. (**A**) Schematic illustration of the synthesis of L-Arg/MB@MP nanotherapy system. (**B_1**) L-Arg/MB@MP with prolonged circulation time in blood after intravenous administration further passively accumulated to tumor site through EPR effect. (**B_2**) A series of chain reactions in tumor cells triggered by GSH and ROS upon L-Arg/MB@MP internalized into cancer cells via endocytosis. (**B_3**) The specific mechanism of L-Arg/MB@MP-mediated photodynamic therapy (PDT) and gas therapy (GT) in the treatment of tumors.

2.3. Characterizations

Transmission electron microscope (TEM) images were acquired on a JEM-100CX electron microscope (JEOL, Japan). Scanning electron microscope (SEM) images, element mapping images, and elements line scanning results were obtained on a field-emission Magellan 400 microscope (FEI Co.). Zeta potential and dynamic light scattering (DLS) measurements were conducted on a Zetasizer Nanoseries (Malvern Instruments, Malvern, UK). The pore size distribution and N_2 adsorption-desorption isotherm of the nanoparticles were determined by Brunauer-Emmett-Teller (BET) analyzer (Micromeritics, ASAP 2020). The drug concentrations in plasma, urine, and feces samples were analyzed using liquid chromatography and mass spectrometry (LC-MS/MS, Agilent, Tokyo, Japan). The Si concentration measurement was conducted by an inductively coupled plasma optical emission spectrometer (ICP-OES, Agilent, Tokyo, Japan).

2.4. Detection of immunogenic cell death (ICD)

The secretion of high mobility group box 1 (HMGB1, Neobioscience Technology Co., Ltd., Shenzhen, China) & ATP and exposure of calreticulin (CRT) were viewed as the biomarkers of the induction of ICD. To observe the exposure of CRT, EMT-6 cells were seeded into confocal dishes and cultured to completely adhered. Specifically, tumor cells were treated with saline (+), MP(+), L-Arg (+), L-Arg@MP(+), L-Arg/MB@MP, MB(+), MB@MP(+), or L-Arg/MB@MP(+) at an equal amount of MB (30 μg/mL) and L-Arg (50 μg/mL) with or without laser irradiation (660 nm, 0.5 W/cm^2, 5 min) incubated for another 24 h. Then the culture medium was removed, and the cells were stained with an anti-calreticulin antibody (Cell Signaling Technology, USA) for 24 h at 4 °C after being fixed. Finally, the tumor cells were incubated with Alexa Fluor 488-conjugated secondary antibody (Beyotime, China) for 1 h and DAPI for 10 min at room temperature. The fluorescence images of calreticulin on the surface of tumor cells were subsequently observed by confocal laser scanning microscope (CLSM) with an excitation wavelength of 488 nm fluorescence-activated cell sorting (FACS) was subjected to quantify CRT-positive cells under a similar process as described in the CLSM observation experiment.

The HMGB1 enzyme-linked immunosorbent assay (ELISA) kit was used to detect the extracellular release of HMGB1. Briefly, MET-6 tumor cells seeded in 6-well plates (1×10^5 cells/well) were cultured with saline (+), MP(+), L-Arg (+), L-Arg@MP(+), L-Arg/MB@MP, MB(+), MB@MP(+), or L-Arg/MB@MP(+) at an equivalent concentration of MB (30 μg/mL) and L-Arg (50 μg/mL) with or without laser irradiation (660 nm, 0.5 W/cm^2, 5 min) for 24 h. The medium was collected for detection of HMGB1 release from the nucleus to the extracellular matrix by ELISA according to the manufacturer's instructions. As for *in vivo* experiment, HMGB1 was detected after homogenization of mice tumor tissues according to the manufacturer's instructions.

Extracellularly released ATP was evaluated by the enhanced ATP assay kit. Briefly, EMT-6 cells were seeded into 96-well plates (1×10^4 cells per well) and cultured for 24 h. The cells were then incubated with saline (+), MP(+), L-Arg (+), L-Arg@MP(+), L-Arg/MB@MP, MB(+), MB@MP(+), or L-Arg/MB@MP(+) at an equivalent concentration of MB (30 μg/mL) and L-Arg (50 μg/mL) for 4 h and irradiated with or without a 660 nm laser (0.5 W/cm^2, 5 min). After an additional 24 h incubation, the cell supernatant was collected and detected by the ATP assay kit according to the manufacturer's protocol. Similarly, *in vivo* experiment, the ATP secretion was detected after homogenization of mice tumor tissues.

2.5. Pharmacokinetic study and biodegradation of L-Arg@MP nanoparticles in vivo

To assess biodistribution of L-Arg@MP nanoparticles and drug metabolism *in vivo*, the LC-MS/MS assay and ICP-OES quantitative assessment were performed in the blood and tissue of SD rats. Specifically, the SD rats were arbitrarily allocated into six groups (n = 5) and administered with MB (2.5 mg/kg), MB@MON (at the equiv. [MB] = 2.5 mg/kg), MB@MP (at the equiv. [MB] = 2.5 mg/kg), L-Arg (1 mg/kg), L-Arg@MON (at the equiv. [L-Arg] = 1 mg/kg), or L-Arg@MP (at the equiv. [L-Arg] = 1 mg/kg) via tail vein injection. Blood samples (0.5 mL) were harvested via tail tip bleeding from mice at a predetermined point in time (5 min, 10 min, 30 min, 60 min, 2 h, 8 h, 24 h, 48 h, and 72 h) after administration and then placed in heparinized tubes immediately. Then, the blood samples were centrifuged (11000g, 5 min) to obtain plasma. The concentration of MB and L-Arg in the plasma was measured by LC-MS/MS method after a series of processes such as protein precipitation and drug extraction. Methylene violet and ubenimex were selected as the internal standards of MB and L-Arg based on the internal standard method for chromatographic quantitative analysis, respectively. Tumor bearing mice were treated according to the same administration method, the mice in free MB, free L-Arg, MB@MP, and L-Arg@MP groups were euthanized, and their heart, liver, spleen, lung, kidney, and tumor tissues were removed for tissue homogenization. Then, the MB and L-Arg were extracted from the tissues and analyzed by LC-MS/MS as described above. The relative drug concentration was represented as the concentration ratio of drugs loaded in the MP group and free drugs. Pharmacokinetic parameters were finally calculated using the DAS 2.0 software (BioGuider Co., Shanghai, China).

To study the degradation behavior of the organosilicon nanoparticles with disulfide bond *in vivo*, the urine and feces of SD rats in the MB@MP group and L-Arg@MP group were collected at a predetermined point in time (0, 2, 4, 8, 24 and 72 h) after administration. Subsequently, the urine and feces were utilized to detect the total accumulated degradation content of Si by ICP-OES.

2.6. Therapeutic effect in animals

The *in vivo* antitumor effect of various therapeutic agents was evaluated on EMT-6 tumor-bearing mice when tumor size reached 100 mm^3. The mice were randomly divided into eight groups (n = 5) and administrated by intravenous injection of saline, MP (+, 2.5 mg/kg), L-Arg (+, 1 mg/kg), L-Arg@MP (+, at the equiv. [L-Arg] = 1 mg/kg), L-Arg/MB@MP (at the equiv. [MB] = 2.5 mg/kg and [L-Arg] = 1 mg/kg), MB (+, 2.5 mg/kg), MB@MP (+, at the equiv. [MB] = 2.5 mg/kg), and L-Arg/MB@MP (+, at the equiv. [MB] = 2.5 mg/kg and [L-Arg] = 1 mg/kg). The 660 nm laser irradiation (0.5 W/cm^2, 5 min) was given to mice in laser-treated groups 24 h after injection. The body weight and tumor volume of the tumor were monitored during the whole treatment period. Also, the living tumor-bearing mice and isolated tumor tissues recordings pictures were taken using a camera. Finally, all mice were sacrificed on day 28, tumors and major organs were excised and preserved in 4% paraformaldehyde. The hearts, livers, spleens, lungs, and kidneys were stained for hematoxylin and eosin (H&E) assay. To investigate the antitumor effect of different therapy, the TUNEL, Ki67, CD31, HIF-1α, ROS staining in tumor tissues was performed according to the manufacturer's instructions. The routine blood tests were conducted to evaluate the biosafety of nanocomposites using the fresh blood of the treated animals.

2.7. Statistical analysis

The statistical calculations of the data were carried out by Prism 6.0 software (GraphPad Software Inc., San Diego, CA, USA) and all data were expressed as mean ± standard derivations (SD). Multigroup analyses were made by one-way analysis of variance (ANOVA) followed by a Student *t*-test and p values below 0.05 were deemed statistically significant.

3. Results and discussion

3.1. Synthesis and characterization of L-Arg/MB@MP

Generally, hypoxia is one of the primary therapeutic obstacles for PDT, whereas hyperoxia promotes the generation of ROS and can enhance the killing effect on tumors [26]. Therefore, we reported biodegradable, large pore-sized, and spherical MON for dual drug delivery to improve hypoxia in solid tumor therapy (Scheme 1). The successful synthesized MON exhibited a uniform spherical morphology and evident mesoporous structure shown in TEM (Fig. 1A) and SEM (Fig. 1B) images. Meanwhile, energy dispersive spectroscopy (EDS) elemental mappings (Figure S1A) and EDS line scans (Figure S1B) of silicon (Si), oxygen (O), sulfur (S), and carbon (C) elements in MON directly showed the homogenous distribution of S and C elements among the layer of MON framework structure, further demonstrating the formation of disulfide bond (-S-S-) have been introduced into MON with a molecular level. During the synthesis process of amino-coated MON (MON-NH_2), the vibration of N–H bonds at the wavenumber of 1650 cm^{-1}, and the absorption bands of S–C and S–S (520-720 cm^{-1}) observed via Fourier

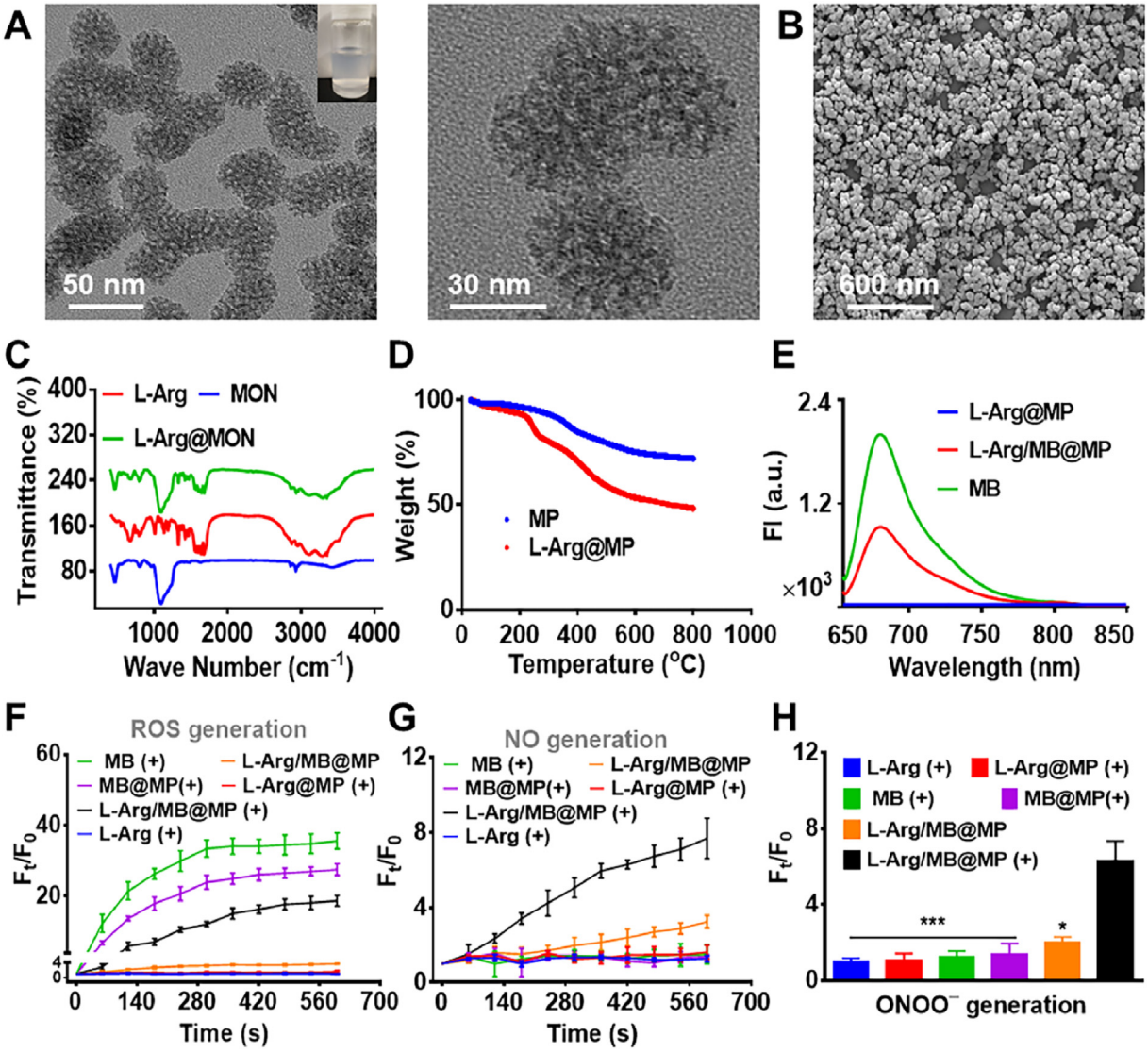

Fig. 1. Preparation and characterization of dual drug delivery system L-Arg/MB@MP. TEM (**A**) and SEM (**B**) images of MON. (**C**) Fourier-transform infrared (FT-IR) spectrum of L-Arg, MON and L-Arg@MON. (**D**) Thermogravimetric analysis (TGA) curves of MP and L-Arg@MP. (**E**) Fluorescence spectra of SOSG with MB, L-Arg@MP, and L-Arg/MB@MP in PBS buffer. (**F**) ROS generation of different samples with a concentration of MB (30 μg/mL) and L-Arg (50 μg/mL) under different irradiation durations by fluorescence spectrum. (**G**) NO generation of different samples with a concentration of MB (30 μg/mL) and L-Arg (50 μg/mL) under different irradiation durations by fluorescence spectrum. (**H**) The generated $ONOO^-$ concentrations arising from the different samples. (+) represented laser irradiation (660 nm, 0.5 W/cm^2, 5 min). Data are shown mean ± SD, n = 3. *p < 0.05 and ***p < 0.005.

Transform Infrared (FT-IR) spectrum proved the formation of the aminated organic framework (Figure S1C) [34]. With the amide reaction of PEG-COOH and the MON-NH_2, the zeta potential was changed from 22.4 ± 1.71 mV to −7.17 ± 2.76 mV (Figure S1E) and the characteristic peaks for PEG showed in the ^{1}H NMR spectrum (Figure S2A) confirming that PEG-COOH has been successfully grafted onto the MON-NH_2 which finally formed to MP. Although the dynamic light scattering (DLS) particle size of MON increased from 50.3 nm to 164.0 nm (Figure S1D) after the modification of PEG, while the surface area and mesoporous in the MP were large enough for drug loading (Figure S2B and **C**). These results clearly indicate that the successful preparation of organosilicon nano-delivery carrier containing disulfide bonds.

To further verify the drug loading capacity of MP, the FT-IR was performed to further characterize whether the NO donor, L-Arg molecule was successfully encapsulated into MON via electrostatic affinity (Fig. 1C). And the L-Arg@MP showed a 25.21% weight loss (Fig. 1D) from the thermogravimetric analysis (TA instruments, USA) compared to MP and a 37.62% loading efficiency evaluated by high-performance liquid chromatography (HPLC). Subsequently, the characteristic spectra of fluorescence (Fig. 1E) confirmed that MB had been encapsulated in the L-Arg@MP which formed the final dual drug-loaded organic nanosystem (denoted as L-Arg/MB@MP). And the loading efficiencies of MB in L-Arg/MB@MP was 16.03% calculated by an ultraviolet/visible (UV/Vis) spectrophotometer (Thermo Scientific, UK) at 662 nm.

3.2. *Biodegradation assay and responsive release study of nanoparticles in vitro*

The breaking response properties of -S-S- makes nanomaterials can specifically respond to the reducing microenvironment in tumor cells or in tumor tissues where has a high concentration of GSH [30,34,35]. To take full advantage of the GSH sensitive properties of -S-S-nanomaterials, as shown in Figure S3A, we introduced the specific framework-incorporated organic R moieties with biologically active -S-S- in the MON, which enables MON to biodegrade in a reducing microenvironment. As expected, the direct introduction of -S-S- into the

framework of MON could realize the GSH-responsive biodegradation of nanocarriers from the images of TEM (Figure S3B). Specifically, there was little variability in the microstructure of MON in simulated body fluids (SBF) in the first 7 days, even after 14 days of biodegradation in SBF, only weak adhesions appeared at TEM images due to the aggregation of MON. Subsequently, the hydrodynamic diameter and polydispersity indices (PDI) records of MP in SBF solution for up to 14 days showed that MP with good dispersion and uniform size (Figure S3C). Notably, the substantial structure collapse and dissolution of MON were clearly seen in the SBF solution containing GSH. The biodegradation rate of MON in high GSH concentration (GSH = 10 mM) was significantly accelerated, and almost no obvious spherical MON by 7 days virtually no further discernible nanoparticles were observed afterward. At the same time, the change of average polydispersity indices (PDI) was monitored in the process of MON degradation which coincide with the data observed by TEM (Figure S3D). In addition, after investigating the biodegradability of MON, the stability of MP was carefully characterized in different biological media (phosphate buffer saline (PBS), saline, RPMI 1640 cell culture medium, fetal bovine serum (FBS), and complete cell culture medium). As shown in Figure S4 and Table S1, there was no obvious precipitation of MP in different media, and the change of particle size and zeta potential showed a reasonable trend [31]. TEM images, hydrodynamic diameter, PDI, and zeta potential directly showed the easy biodegradation behavior of MON in reducing microenvironment containing GSH, which was also expected to be contributed to the responsive release ability of L-Arg/MB@MP.

To evaluate the potential of MP as ideal drug delivery carriers for tumor synergistic therapy of GT and PDT, L-Arg/MB@MP were incubated in a normal physiological environment (SBF) and SBF containing GSH ([GSH] = 5 and 10 mM) and then the GSH triggered drug release behavior was assessed by the release profiles of L-Arg and MB. It seemed that MB and L-Arg could be successfully released from the macropores of L-Arg/MB@MP nanocomposites, respectively (Figure S5A-**C**). There was almost no L-Arg and MB release in SBF before the first 6 h, followed by a slow release over 24 h. The cumulative release rate of L-Arg and MB at pH 7.4 in SBF without GSH was about 7.36% and 13.46% after 24 h of incubation, which suggested that PEGylation nanoparticles could protect the drug encapsulated in the system without leakage under normal physiological conditions. Furthermore, the GSH sensitive release behavior of L-Arg/MB@MP under the reducing conditions ([GSH] = 5 and 10 mM) was also evaluated. L-Arg and MB showed a burst release before 4 h, followed by a rapid release over 16 h and finally gradual sustained release until 24 h in SBF with GSH. The L-Arg and MB release behavior was in an obvious GSH-sensitive manner (Figure S5B and **C**), where the cumulative release at GSH (10 mM) seemed to be higher than that at GSH (5 mM). And over a 24 h period the cumulative release was approximately 76.74% ([GSH] = 5 mM) and 96.53% ([GSH] = 10 mM) for L-Arg, 88.96% ([GSH] = 5 mM) and 98.14% ([GSH] = 10 mM) for MB. In contrast, in SBF without GSH, the release of L-Arg and MB was less than 15% in 24 h. These results indicated that L-Arg/MB@MP were responsive to GSH, and responsive degradation of GSH unpacked the organic macroporous nanostructure [30], thereby quickly releasing the contained drugs, consistent with the TEM observations. These results clearly demonstrated that L-Arg/MB@MP with regular morphology had excellent stability under normal physiological circumstances, but exhibited sensitive degradable characteristics under reducing conditions.

3.3. ROS and NO generation properties of L-Arg/MB@MP under cascade reaction

MB-based nanosystem was previously reported as activatable photosensitizer agents for selective PDT [36–39]. Therefore, the *in vitro* photodynamic performance of MB-based L-Arg/MB@MP was comprehensively evaluated. As shown in Figure S6A, free MB and MB@MP displayed a concentration-dependent relative fluorescence intensity (F_t/F_0) change upon 660 nm laser irradiation (0.5 W/cm^2, 5 min). Specifically, the F_t/F_0 of free MB and MB@MP rapidly increased to 38 and 23 folds of the initial value after laser irradiation at the 30 μg/mL concentration of MB, respectively, which verified the ability of MB production ROS. Additionally, the change of irradiation time presented an analogous trend concentration-dependent ROS generation performance (Fig. 1F). Moreover, only when the laser source and photosensitizer were paired can the entire nanosystem generate enough ROS for subsequent PDT, because the emission of the laser must match the wavelength absorption of the photosensitizer to be effectively activated [40]. And the lower F_t/F_0 of MB loaded in MP in comparison with free MB was mainly owing to the encapsulation of MB which was well consistent with the fluorescence spectroscopy (Fig. 1E). It could be interpreted that MB was encapsulated inside the hydrophobic cores of nanoparticles under physiological condition (pH 7.4), where its fluorescence was quenched by the aggregation effects. While the L-Arg/MB@MP(+) exhibited a weaker F_t/F_0 were due to ROS consumption by L-Arg. Furthermore, the NO production of L-Arg/MB@MP under different concentrations of L-Arg was evaluated by the DAF-FM DA fluorescent probe. As shown in Figure S6B, the F_t/F_0 of NO in L-Arg/MB@MP(+) group was obvious concentration-dependent when L-Arg concentration was lower than 70 μg/mL, while the F_t/F_0 of L-Arg/MB@MP(+) decreased gradually as the concentration of L-Arg over 70 μg/mL, suggesting that the lower NO generation. This was due to the fact that, while the amount of L-Arg was gradually increased in this experiment, the amount of MB remained constant. As MB was continuously consumed, the resulting ROS decreased gradually, and thus the ROS that could be used to oxidize L-Arg decreased as well. Eventually, the NO produced by L-Arg would decrease. Simultaneously, among different treatment groups at equivalent drug concentration ([MB] = 30 μg/mL, [L-Arg] = 50 μg/mL), only the L-Arg/MB@MP(+) group was observed a sustained increasing F_t/F_0 with laser irradiation duration (Fig. 1G). Compared with the constantly amount of NO generated by L-Arg/MB@MP(+), there was an almost no production of NO was monitored in the free MB and free L-Arg group. These results confirmed the ROS generation capacity of L-Arg/MB@MP, and produced ROS could spontaneously react with L-Arg to generate NO. Overall, L-Arg and ROS were two essential factors to produce NO. Also, $ONOO^-$ produced by the cascade reaction of ROS and NO was detected by an $ONOO^-$ fluorescent probe under various treatments presented in Fig. 1H. A large amount of $ONOO^-$ generated by L-Arg/MB@MP(+) verified that the nanosystem could amplify the therapeutic effect of PDT because of the stronger toxicity of RNS [41].

After preliminary investigation on the effective ROS production triggered NO release, the critical role of ROS in the consecutive oxidation reaction was proceeded to explore. Firstly, different concentrations of Vc as a typical quencher of ROS were incubated with L-Arg/MB@MP under 660 nm laser irradiation (0.5 W/cm^2, 5 min). Then the F_t/F_0 value of L-Arg/MB@MP was collected shown in Figure S7A to display the release behavior of NO at different concentrations of Vc. Under laser irradiation, the F_t/F_0 of L-Arg/MB@MP presented a slow growth with the increased concentration of Vc. When the concentration of Vc reached 120 mg/L, the released ROS almost completely depleted by Vc which result in NO production hardly being observed. In contrast, the NO generation of L-Arg/MB@MP grew approximately linearly when Vc was absent. Additionally, appropriate laser irradiation was required for the generation of ROS during PDT [38], which indicated that light was also necessary for NO generation. The L-Arg/MB@MP could demonstrate an accurate reaction to the release of NO under the ON-OFF condition of 660 nm laser irradiation, as illustrated in Figure S7B. As the laser irradiation duration was canceled, the rate of NO production remained rather stable indicating the ability of L-Arg/MB@MP to achieve precisely controlled NO release. More importantly, GSH-sensitive L-Arg/MB@MP could deplete GSH (Figure S7C) and finally sensitized PDT because GSH could reduce ROS and prevent ROS-mediated cell death [42]. The results revealed that L-Arg/MB@MP can achieve the controlled release of ROS and NO based on precise regulation of the cascade reactions.

3.4. In vitro cellular uptake and lysosomal escape behavior of nanoparticles

Effective cellular uptake is the premise for L-Arg/MB@MP to exert their anticancer therapeutic effects, so FITC was loaded into MP to prepare the FITC@MP for CLSM imaging and FACS analysis. The green fluorescent signal from FITC@MP was observed in EMT-6 cells at 2 h post-coincubation (Fig. 2A), indicating nanoparticles were efficiently and continuously endocytosed by tumor cells. Quantitative analysis also illustrated the endocytosis amount of FITC@MP increased with extended incubation time (Figure S8A), and the cellular uptake efficiency in 4 h was 3-fold more than that of in 2 h (Figure S8B). Generally, the visualization of lysosomal localization or escape ability is highly essential to assess and enhance the therapeutic impact of drug delivery systems since lysosomes are the major physiological barrier in the process of drug delivery systems further performing their therapeutic role [43]. The interaction of FITC@MP with tumor cells had been investigated by a colocalization study using LysoTracker Red. As shown in Fig. 2B, with the incubation period prolonged, FITC@MP displayed a well-defined time--dependent rise in fluorescence intensity proved that the endocytosis amount of FITC@MP increased consistent with Fig. 2A. Simultaneously, the observed yellow colocalization regions of the green fluorescence from FITC@MP and the red fluorescence from LysoTracker Red also exhibited an increasing trend and peaked at 4 h, then progressively diminished. Subsequently, the colocalization analysis performed using ImageJ also implied a continuous accumulation of FITC@MP into the lysosomes of MET-6 tumor cells before escaping (Figure S9). The results demonstrated that FITC@MP was able to escape the lysosomes after efficient cell internalization, avoiding any potential degradation and delivering high-efficacy therapy.

3.5. Intracellular ROS/NO level of L-Arg/MB@MP

Inspired by the good performance characteristics cascade reactions of L-Arg/MB@MP in solution, the detection of ROS and NO *in vitro* was further carried out respectively using DCFH and DAF-FM DA fluorescent probes by CLSM and FACS analysis to visualize the intracellular ROS/NO production of L-Arg/MB@MP. As shown in Fig. 2C, typical ROS green fluorescence can be observed after tumor cells were co-incubated with free MB(+). While the MB@MP(+) showed higher fluorescence intensity indicating that the PEGylated nanoparticles could promote more cellular endocytosis. And the GSH depletion caused by the biodegradable MP will further promote the production of ROS. Notably, L-Arg/MB@MP(+) generated fluorescence with lower intensity and smaller area compared to the MB@MP(+) group (Figure S10A and **B**), which can be explained by the consumption of ROS for L-Arg oxidation.

To verify whether ROS can oxidize L-Arg and further promote NO production, the level of intracellular NO production was tested by CLSM.

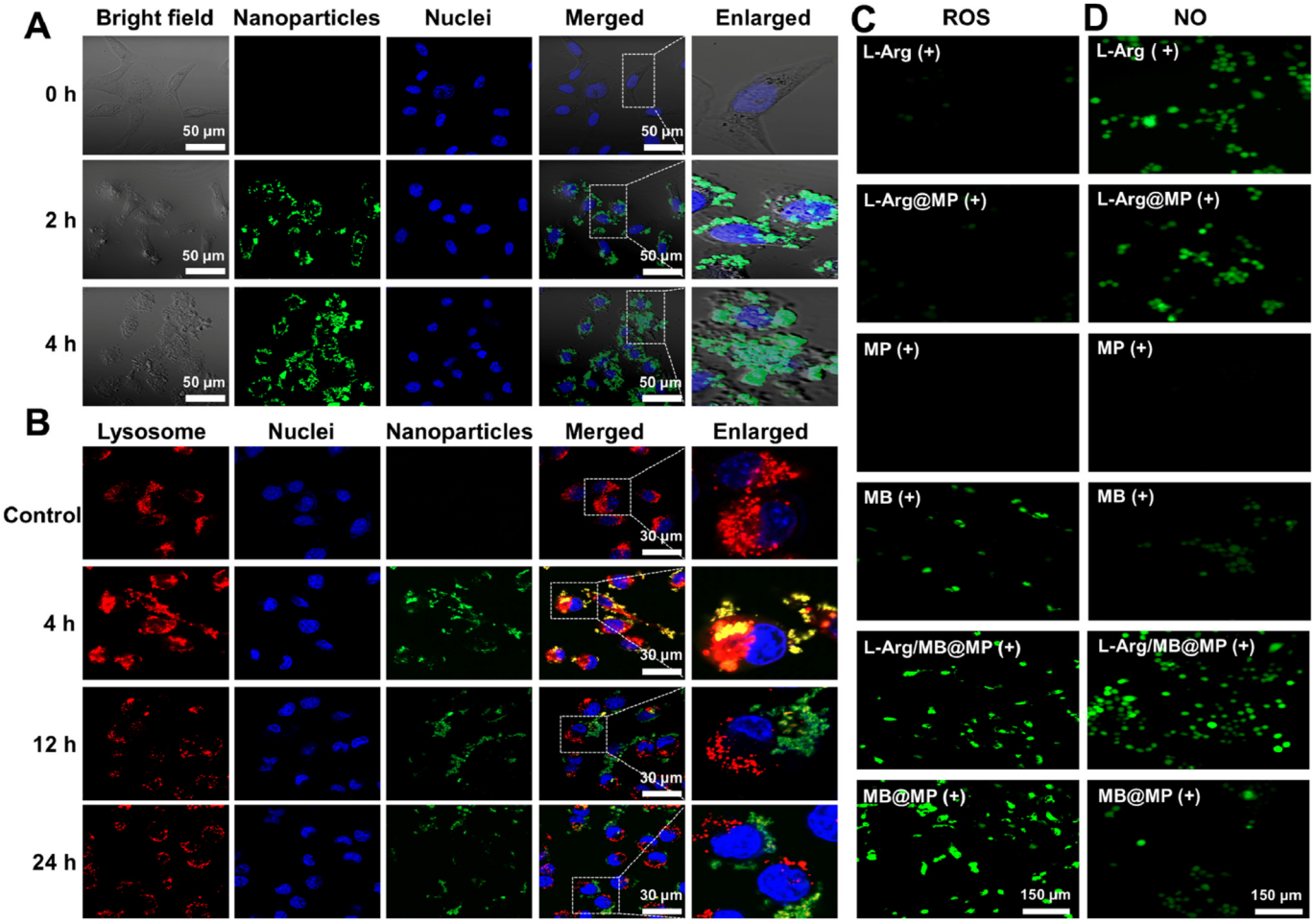

Fig. 2. Cellular uptake and lysosomal escape of nanoparticles, and detection of indicators of ROS/NO *in vitro*. (**A**) Representative CLSM images of EMT-6 cells incubated with FITC@MP at various time points. Green channel: FITC labeled particles; Blue channel: DAPI. Scale bar = 50 μm. (**B**) Representative CLSM images of lysosomal escape of FITC@MP in EMT-6 cells after 4 h, 12 h, and 24 h of co-incubation. Red channel: LysoTracker red-stained lysosomes; Green channel: FITC-labeled particles; Blue channel: DAPI. Scale bar = 30 μm. (**C**) Representative CLSM images of ROS produced by EMT-6 cells after different treatments (scale bar = 150 μm). (**D**) Representative CLSM images of NO produced by EMT-6 cells after different treatments (scale bar = 150 μm). (+) represented laser irradiation (660 nm, 0.5 W/cm^2, 5 min).

As expected, L-Arg/MB@MP revealed the superior NO fluorescence compared with the other groups under irradiation (Fig. 2D), qualitatively data also proved that L-Arg/MB@MP with 660 nm laser irradiation could effectively release NO (green signal), suggesting the successful oxidation of L-Arg by ROS (Figure S11A and **B**). Conversely, the MP group exhibited virtually no fluorescence upon 660 nm light irradiation. L-Arg served as a natural NO donor has been reported for its good ability of NO production under the catalysis of inducible NO synthase enzyme [16]. More importantly, L-Arg can also be transformed into NO via oxidization of ROS including endogenous H_2O_2 and $^1O_2$. Compared with normal tissue, the content of H_2O_2 in tumor cells tends to be higher. So, despite the absence of photosensitizers, weak green fluorescence of NO was still observed in tumor cells treated with L-Arg (+) and L-Arg@MP(+) groups compared with L-Arg/MB@MP(+) groups. These findings proved that NO could not be produced in the absence of any element including oxidizing agent and NO donors. Even more significant, under 660 nm laser irradiation, the GSH consuming biodegradable L-Arg/MB@MP could release both ROS and NO, laying the groundwork for synergistic PDT-GT cancer therapy.

3.6. *In vitro synergistic PDT-GT therapy study*

Encouraged by the appealing ROS and NO generation properties of L-Arg/MB@MP, the synergistic therapeutic performance of L-Arg/MB@MP was further systematically evaluated. It is generally known that low toxicity is essential for future applications as a kind of biological nanomaterial and medication carrier [44]. Therefore, the toxicity of L-Arg/MB@MP was measured and analyzed by the CCK-8 experiment. Considering the negligible cytotoxicity of the 660 nm lasers irradiation with the power of 0.5 W/cm^2 for 5 min, the corresponding laser intensity was applied to evaluate the biosafety of MON and MP (Figure S12). The cell viability of 4T1 and EMT-6 cells treated with MON (Figure S13A and **B**) or MP (Figure S13D and **E**) were more than 80% when the nanocarrier concentration was higher than 240 μg/mL. And following PEG modification, MP exhibited improved biosafety to normal cells (HUVEC), owing to PEG ability to increase nanoparticle biocompatibility (Figure S13C and **F**).

Having confirmed a satisfactory biosafety property of MP *in vitro*, we continued to evaluate the subsequent tumor cell killing ability of free L-Arg and free MB (Figure S14). Even though the L-Arg concentration steadily rose, the tumor cell survival ratio remained over 80%, indicating that the NO donor as an endogenous amino acid alone cannot induce enough cell death without the activation of ROS (Figure S14A). However, the cytotoxicity of free MB presented a concentration dependence under 660 nm laser irradiation (0.5 W/cm^2, 5 min) (Figure S14B). In addition, the *in vitro* combined therapeutic effects of ROS and NO was then studied by incubating EMT-6 cells with L-Arg/MB@MP under the same conditions. As shown in Figure S15C, MB@MP(+) exhibited stronger cancer cell inhibition than free MB(+), which was due to the size effect of nanoparticles that could facilitate drug endocytosis. Furthermore, under the treatment of L-Arg/MB(+), tumor cells had greater toxicity than that of free MB(+), and the L-Arg/MB@MP(+) could effectively inhibit the EMT-6 cells with the L-Arg and MB concentrations as low as 32 and 50 μg/mL. But without laser irradiation, the cell survival ratio in L-Arg/MB@MP group was approximately as high as 83% indicating that the drug delivery system without laser irradiation was harmless to cells under the same concentration conditions. It is worth noting that the powerful synergistic therapy of the L-Arg/MB@MP(+) group also can be found in live/dead cell staining assay (Figure S15A and **B**).

As one of the predominant characteristics of malignant tumor cell proliferation in cancer development, dysregulation of cell cycle progression and cell apoptosis is critical for cell proliferation [45]. So, FACS and western blot analysis were utilized to verify whether the mechanism of L-Arg/MB@MP(+) affecting cell proliferation was associated with cell cycle arrest and induction of apoptosis. Firstly, EMT-6 cells were collected and stained after treatment in different therapy groups and finally evaluated by FACS. It could be observed that tumor cells treated with MB(+), MB@MP(+), L-Arg/MB(+), or L-Arg/MB@MP(+) had similar G2/M phase cell cycle arrest compared with the control (Fig. 3B), which suggested the induction of ROS production and DNA damage responses by MB. Notably, codelivery of L-Arg and MB by MP under laser irradiation exhibited the strongest effects on cell cycles as shown in Fig. 3C. The G2/M phase of L-Arg/MB@MP(+) increased to 35.25% compared to L-Arg/MB@MP (11.3%), which suggested L-Arg/MB@MP(+) could significantly block the EMT-6 cells into the G2/M phase. Simultaneously, the effect of L-Arg/MB@MP(+) on the expression of cell cycle-related proteins (cdc2, cdc25c, and cyclin B) were further explored through western blot analysis (Fig. 3D). The obvious downregulation of cdc2, cyclin B, and cdc25c explained that L-Arg/MB@MP(+) mediated PDT-GT combined therapy could induce oxidative DNA damage, which in turn promote the phosphorylation of cdc25c, leading to the inhibition of the binding of cdc2 and cyclin B, and finally block G2 checkpoint. Quantitative western blot analysis of cdc2, p-cdc2, cyclin B, cdc25c, p-cdc25c showed the similar phenomenon (Figure S16A-E). And a schematic representation of the cell cycle-arrest signaling pathway was shown in Fig. 3A.

In addition, the survival energy of tumor cells mainly depended on adenosine triphosphate (ATP) produced in mitochondria, and the membrane potential of mitochondria usually changed during cell early apoptosis [46]. Therefore, the influence of various treatments on the mitochondrial membrane potential of EMT-6 cells was explored via JC-1 probes. As shown in Figure S17, tumor cells treated with MB(+), MB@MP(+), L-Arg/MB(+), or L-Arg/MB@MP(+) obviously appeared mitochondrial membrane potential changes (red-green color changing). The quantitative results of red/green fluorescence intensity were further determined by FACS analysis to exhibit the specific changes of mitochondrial membrane potential (Figure S18). Compared to MB@MP(+), L-Arg/MB@MP(+) that effectively integrated synergistic therapy caused more severe red-green discoloration, proving that L-Arg/MB@MP(+) could remarkably impact mitochondrial activity and eventually resulted in cells apoptosis. Besides, massive early-stage apoptosis appeared in the MB@MP(+) group as compared to MB(+), demonstrating that the MP can not only promote the endocytosis of free MB, but more importantly, the degradation of silicone carriers can consume the high GSH in tumor cells, which can further amplify the therapeutic effect of PDT.

To understand the mechanistic cell death by apoptotic pathways, subsequently, the percentage of living cells, early apoptotic cells, late apoptotic cells, and necrotic cells were identified via FACS assay employed with an Annexin V-FITC/PI cell apoptosis kit. As shown in Fig. 3E, negligible apoptosis was observed in L-Arg (+) and L-Arg@MP(+) group consistent with cell cycle and cell proliferation results. And upon 660 nm laser irradiation, the percentages of early and late apoptotic cells increased to 48.70 ± 4.40%, 60.19 ± 3.08%, 69.15 ± 5.10%, and 88.41 ± 1.55% for MB(+), MB@MP(+), L-Arg/MB(+), and L-Arg/MB@MP(+), respectively (Fig. 3F). Remarkably, the significant higher apoptosis appeared in L-Arg/MB@MP(+) group compared to MB@MP(+) group (Figure S19), indicating that the considerable improvement in PDT was due to ROS converting L-Arg into NO, which was further oxidized by ROS to promote more toxic RNS production. Furthermore, in EMT-6 tumor cells treated with L-Arg/MB@MP(+), the most expression of Bcl-2 was downregulated, whereas the expression of Bax, p53, cleaved caspase-3, and caspase-3 were upregulated compared to the control (PBS group) (Fig. 3G and Figure S20), which suggested that L-Arg/MB@MP(+) cause mitochondrial damage via Bcl-2 suppression and Bax induction (Fig. 3A). These results proved that L-Arg/MB@MP(+) could realize PDT with GT sensitization under external light stimulation, and ultimately achieve more effective synergistic therapy. Taken together, these results proved the efficient inhibiting cell proliferation and inducing apoptosis of L-Arg/MB@MP(+), which is beneficial for subsequent promoting immunogenic cell death.

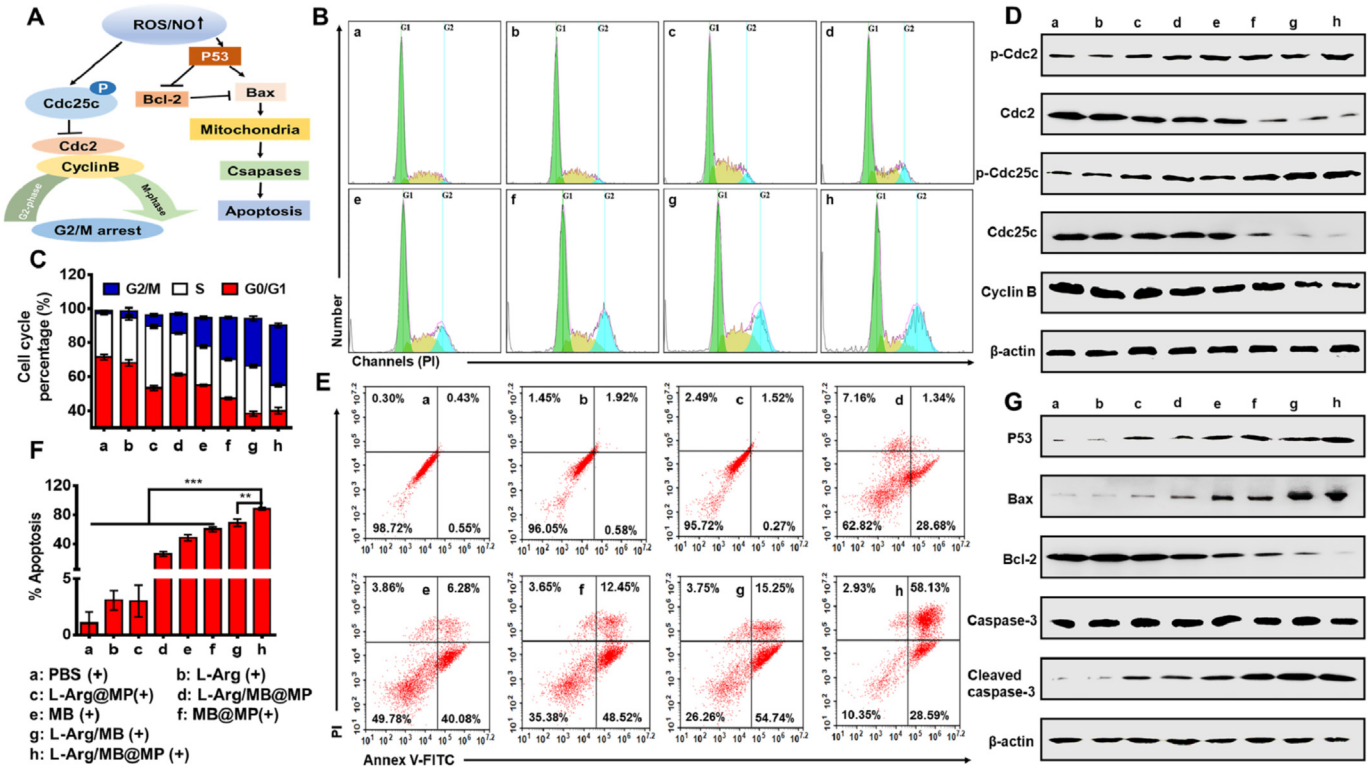

Fig. 3. Intrinsic signal pathways analysis. (**A**) Schematic diagram of L-Arg/MB@MP causing cell cycle arrest and inducing apoptosis via signaling pathways *in vitro*. (**B**) Flow cytometric analysis of cell cycle after various treatments. (**C**) The percentage of each phase on the cell cycle in different treatment groups. (**D**) Western blot analysis of key proteins of cell cycle and downstream pathway proteins in EMT-6 cells. (**E**) Flow cytometry-based apoptosis assay using Annexin V-FITC/PI co-staining. (**F**) The percentages of apoptotic cells were assessed by flow cytometry. (**G**) Western blot assays for detecting apoptosis-related and antiapoptotic proteins expression in EMT-6 cells treated at different conditions. (+) represented laser irradiation (660 nm, 0.5 W/cm^2, 5 min). Data were shown mean ± SD, n = 3. **p < 0.01 and ***p < 0.005.

3.7. Induction of immunogenic cell death in vitro and in vivo immunosuppression-relieving effects

Currently, increasing emphasis is being placed on the use of certain stress agents that might elicit ICD in tumor cells [47]. Recent studies have shown that PDT can elicit an adaptive immune response by inducing ICD, thereby expanding the mechanism of PDT in clinical therapy [48]. It is necessary to explore whether the oxidative stress caused by PDT-GT drives immunological responses of tumor cell immunogenicity. Therefore, CRT expression, HMGB1 release, and ATP secretion were measured to confirm whether PDT-GT could induce cancer immunity via the ICD effect. As shown in Fig. 4B, tumor cells treated with MB(+), MB@MP(+), and L-Arg/MB@MP(+) exhibited intense green fluorescence compared to cells treated with saline, MP(+), L-Arg (+) and L-Arg@MP(+), indicating higher cell-surface exposure of CRT. The quantitative analysis conducted by FACS also displayed the superiority of L-Arg/MB@MP(+) in inducing ICD (Fig. 4C). Specifically, PDT-GT combined therapy group of L-Arg/MB@MP(+) induced 66.70 ± 3.61% CRT positive cells, while only 13.07 ± 2.91% and 41.27 ± 2.39% of CRT expression were induced by treatment with L-Arg@MP(+) or MB@MP(+) alone, respectively, suggesting that ROS and RNS-mediated synergistic therapy induce tumor cells to undergo immune-stimulatory immunogenic cell death.

In addition, the release of HMGB1 from tumor cells to extracellular matrix after being treated with L-Arg/MB@MP(+) was continued to investigate. ICD could encourage the movement of HMGB1 from the nucleus to the periphery of cells. As shown in Fig. 4D, HMGB1 released from cells treated with L-Arg/MB@MP(+) was about 3.3-fold more than that of L-Arg/MB@MP, indicating that laser irradiation promotes the secretion of HMGB1. Moreover, the amount of HMGB1 released from tumor cells treated with L-Arg/MB@MP(+) was up to 1159.33 ± 122.87 pg/mL, which was the highest among all treatment groups. Subsequently, the ATP assay was subjected to access the release behavior of APT to further confirm the ICD effect (Fig. 4E). Both MP(+) and L-Arg@MP(+) treated cells showed extremely low secretion levels of ATP compared to the L-Arg/MB@MP(+) group, indicating that MP was an excellent biosafety carrier and L-Arg as an endogenous NO donor significantly caused oxidative stress under the stimulation of ROS. In summary, tumor cells were stimulated by PDT-GT to produce dying apoptotic cells that express CRT and secrete ATP and HMGB1, which were considered as “find me” and “eat me” signals to attract and recruit phagocytes (Fig. 4A). The process will finally augment DCs maturation and facilitate antitumor T-cell activation [47,49].

To further investigate the influence of tumor-associated antigens exposure or release on DCs maturation, the tumor-draining lymph nodes in EMT-6 tumor-bearing mice after being treated with various therapeutic agents were collected to detect the population of $CD11c^+CD80^+CD86^+$ DCs by FACS analysis. As shown in Fig. 4F and **G**, the amounts of mature DCs ($CD11c^+CD80^+CD86^+$) relative to all DCs ($CD11c^+$) in tumor-draining lymph nodes for MB(+), MB@MP(+), or L-Arg/MB@MP(+) treated mice were 29.24 ± 2.01%, 37.78 ± 1.76%, and 58.16 ± 4.17%, respectively, which were significantly higher than that of saline-treated mice (10.78 ± 1.92%). Moreover, after laser irradiation, L-Arg/MB@MP(+) remarkably enhanced the ratio of mature DCs higher than that in the L-Arg/MB@MP (22.56 ± 2.73%) group indicating laser irradiation was essential for L-Arg/MB@MP to induce ICD to enhance tumor immunogenicity. All these results indicated that PDT-GT mediated amplification of oxidative stress could induce potent immunogenicity and DCs maturation, which would potentially relieve the immunosuppressive microenvironment and activate systemic anticancer immunity.

It is well known that the microenvironment in many kinds of solid

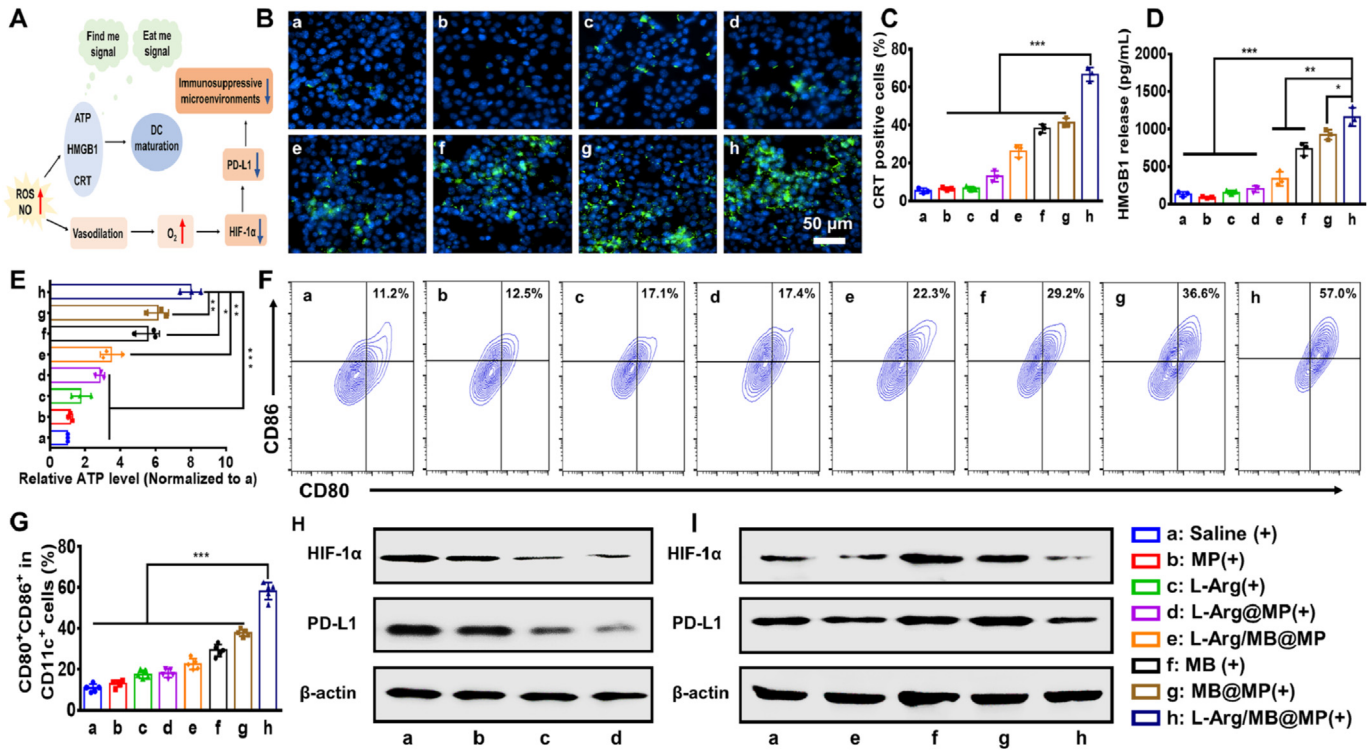

Fig. 4. *In vitro* immunogenic cell death (ICD) inductions, *in vivo* hypoxia alleviation, and *in vivo* dendritic cells (DCs) maturation. (**A**) Scheme of the ICD and alleviation of hypoxia. (**B**) Immunofluorescence staining of CRT expressions on EMT-6 cell surfaces after different treatments (scale bar = 50 μm). Green channel: calreticulin; Blue channel: DAPI. (**C**) Flow cytometry analyses of the exposed CRT on the surface of EMT-6 cells after various treatments (n = 3). (**D**) Detection of high mobility group protein B1 (HMGB1) release by ELISA kit (n = 3). (**E**) ATP release by EMT-6 cells after various treatments (n = 3). (**F**) Representative flow cytometry analysis for CD80 and CD86 expression in the lymph nodes of tumor-bearing mice after being treated with different treatments (gated on $CD11c^+$ cells). (**G**) Statistical analysis of (F) (n = 5). (**H, I**) Representative western blot analysis of HIF-1α and PD-L1 in EMT-6 tumor-bearing mice after various treatments. (+) represented laser irradiation (660 nm, 0.5 W/cm^2, 5 min). Data were shown mean ± SD. *p < 0.05, **p < 0.01, and ***p < 0.005.

tumors is hypoxic. In particular, the continuous utilization of oxygen during PDT for generating cell-damaging ROS further aggravates the tumor hypoxia, which severely hampers efficient ROS generation and resulting in unsatisfactory PDT efficiency [50]. To verify the hypoxia relief ability of L-Arg/MB@MP, various therapeutic agents with saline as control was intravenous injected into tumor-bearing BALB/c mice respectively. Firstly, HIF-1α expression in EMT-6 cells after being treated with different concentrations of MB@MP(+) was assessed by western blot assay. HIF-1α expression increased with the addition of MB@MP(+) in a concentration-dependent manner as described in Figure S21A and B. Meanwhile, the overexpressed HIF-1α in tumor cells could significantly upregulate the PD-L1 protein expression finally resulting in an immunosuppressive tumor microenvironment (Figure S21 A and **C**). To further investigate the effect of NO donors in alleviating hypoxia in the tumor microenvironment, tumor tissues from EMT-6 tumor-bearing mice treated with various nanoparticles were extracted and analyzed by western blot for the expression of HIF-1α and PD-L1 protein. The expression of HIF-1α and PD-L1 in tumor tissue of mice was slightly downregulated owing to the treatments of L-Arg (+) and L-Arg@MP(+) in comparison with saline (+) and MP(+) group (Fig. 4H). Therapy containing only L-Arg can downregulate the expression of HIF-1α and PD-L1 indicated that L-Arg delivered to mice through vein injection was catalyzed by nitric oxide synthase, and finally formatted NO. It is well known that NO as an important regulation messenger of vascular tone could realize tumor hypoxia relief [51]. Especially, L-Arg/MB@MP(+) treatment demonstrated the most significant suppression of HIF-1α and PD-L1 expression in tumor tissues of mice compared to L-Arg/MB@MP, MB(+), MB@MP(+) group, most likely due to a synergistic effect of tumor growth-suppression by PDT and alleviation of the hypoxic condition by GT (Fig. 4I and Figure S22). These results evidenced that the L-Arg/MB@MP as a novel type of nanomedicine could effectively deplete GSH, and thus generate enough ROS to significantly amplify the oxidative stress *in vivo*. On the other hand, the precisely controlled release of NO in the tumor site not only can contribute to alleviating hypoxia at the tumor site but also reversing the immunosuppressive TME.

3.8. *In vivo imaging and pharmacokinetics*

In vivo bioimaging function plays an essential role in accurate diagnosis and therapy of tumors. Next, the biodistribution of this nanoplatform in EMT-6 tumor-bearing mice were investigated by detecting the fluorescence of ICG. As time elapsed, the ICG fluorescence signal in the tumor site of ICG@MP group became stronger than that of free ICG group (Fig. 5A). In addition, free ICG preferred to accumulate in the abdomen, indicating faster elimination of free drugs while ICG@MP gradually accumulated at the tumor site by EPR effect. The quantitative mean fluorescence signal analysis also proved that the PEG-modified nanoparticles significantly enhanced the accumulation of drugs in the EMT-6 tumor model *in vivo* (Fig. 5B). The *ex vivo* imaging and the corresponding quantification data of isolated tumors further confirmed the considerable high tumor accumulation of ICG@MP (Figure S23A and **B**). While in the normal organs, especially the liver and kidney, mean fluorescence intensity was relatively increased in the ICG@MP treated mice due to the metabolism of ICG@MP in the body. The above results revealed the excellent tumor accumulation of MP, which was crucial for their *in vivo* application.

To further evaluate the pharmacokinetic characteristics of this drug delivery system, the LC-MS/MS was utilized to quantitatively analyze the

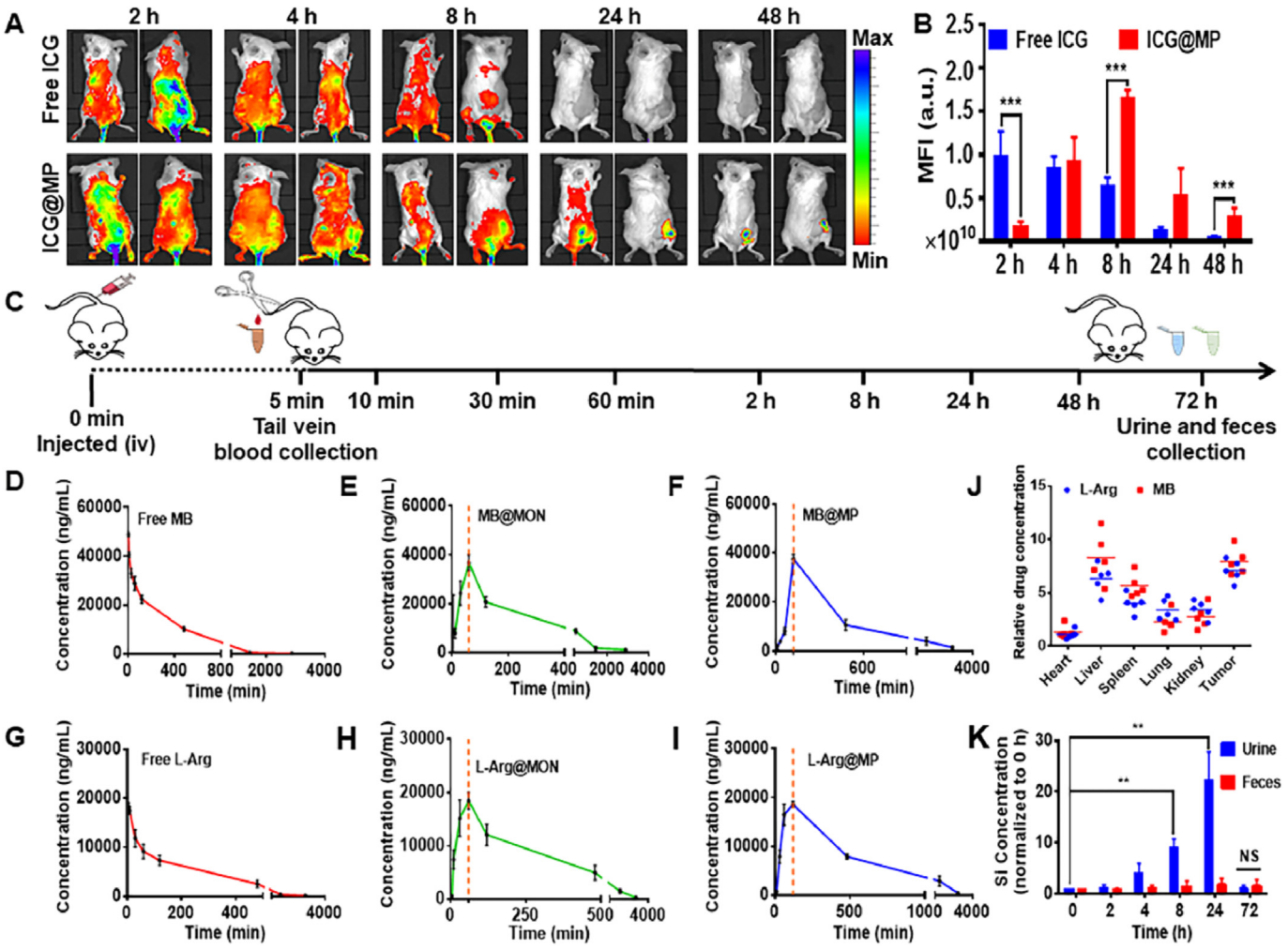

Fig. 5. Nanosystem biodistribution and drug metabolism *in vivo*. (**A**) *In vivo* fluorescence imaging of EMT-6 tumor-bearing mice receiving free ICG and ICG-loaded nanoparticles via i. v. injection. (**B**) Quantitative analysis for the fluorescence intensity of tumor sites in (A) (n = 5). (**C**) Schematic showing the treatment schedule in SD rats after different drugs administration. At 5 min, 10 min, 30 min, 60 min, 2 h, 8 h, 24 h, and 48 h, the tail of the rats was cut for blood collection. The urine and feces were collected at 0 h, 2 h, 4 h, 8 h, 24 h, and 72 h. Pharmacokinetic analysis of peak serum MB concentration in rats detected after free MB (2.5 mg/kg) (**D**), MB@MON ([MB] = 2.5 mg/kg) (**E**), and MB@MP ([MB] = 2.5 mg/kg) (**F**) ravenous injection (n = 5). Pharmacokinetic analysis of peak serum L-Arg concentration in rats detected after free L-Arg (1 mg/kg) (**G**), L-Arg@MON ([L-Arg] = 1 mg/kg) (**H**), and L-Arg@MP ([L-Arg] = 1 mg/kg) (**I**) ravenous injection (n = 5). (**J**) Tissue distribution of MB and L-Arg in mice after MB@MP and L-Arg@MP administration (n = 5). (**K**) Si elemental distribution in urine and feces after MB@MP and L-Arg@MP administration at different time points (n = 5). Relative drug concentration had presented the ratio of drug concentration in the MB@MP group to that in the MB group, or the ratio of drug concentration in the L-Arg@MP group to that in the L-Arg group. MFI: mean fluorescence intensity. Data were shown mean ± SD. NS: no significant difference ($p > 0.05$). **$p < 0.01$ and ***$p < 0.005$.

amount of L-Arg and MB in the plasma of SD rats in response to various time points after intravenous administration (Fig. 5C). Methylene violet (Figure S24B) and ubenimex (Figure S24D) were chosen as the internal standard (IS) given its similar chemical structure to MB (Figure S24A) and L-Arg (Figure S24C), respectively. Meanwhile, MS responses were obtained in the positive ion electrospray ionization mass spectra under the multiple reaction monitoring modes, and *m/z* 284 for MB, *m/z* 343 for methylene violet, *m/z* 175 for L-Arg, and *m/z* 309 for ubenimex were used for quantification (Figure S25A-D). The representative chromatograms of MB and methylene violet obtained after administration of different MB formulations were shown in Figure S26. And the chromatograms of L-Arg and ubenimex with similar high selectivity and sensitivity were also observed in Figure S27.

A highly rapid, sensitive, accurate, and repeatable LC-MS/MS method was developed as above described to simultaneously characterize the concentrations of MB and methylene violet, or L-Arg and ubenimex in rat plasma, respectively. Then the pharmacokinetics study was successfully applied to evaluate the metabolic mechanism and process of the nanodrugs *in vivo*. As shown in Fig. 5D and **G**, the mean plasma concentration-time curves for free MB and free L-Arg suggested free drugs undergo a quick clearance phase before 6 h after intravenous administration. However, MB@MON and L-Arg@MON presented a significantly extended blood circulation time compared to the free drugs, although the macropores of MON could lead to drug leakage (Fig. 5E and **H**). It was found that the plasma level of MB and L-Arg in the MB@MP and L-Arg@MP treated mice was gradually increased, peaked at 1–2 h, and slowly decreased over 48 h (Fig. 5F and **I**). Besides, PEGylation drug-loaded nanoparticles demonstrated much longer blood circulation time and exhibited reduction-triggered release of drugs compared to the above formulations. The incredible stability of MB@MP and L-Arg@MP in blood circulation might mainly be due to the desired surface charge and particle size as well as the hydrophilic PEG shell [52].

Pharmacokinetic parameters for MB, methylene violet, L-Arg, and ubenimex were subsequently analyzed by DAS.20 and shown in Table S2.

Specifically, MB@MP was found to have a long $T_{1/2}$ (7.59 ± 1.07 h), a slow clearance (0.21 ± 0.34 L/h/kg), and a high AUC_{0-t} (294692.21 ± 883.54 ug/L*h) compared to free MB and MB@MON. L-Arg@MP was found to have a long $T_{1/2}$ (8.59 ± 1.36 h), a slow clearance (0.14 ± 0.21 L/h/kg), and a high AUC_{0-t} (253811.20 ± 8926.09 ug/L*h) compared to free L-Arg and L-Arg@MON. Most notably, MB and L-Arg revealed more distribution in tumor site following MB@MP and L-Arg@MP administration, respectively (Fig. 5J), which was consistent with the results of *in vivo* fluorescence imaging (Fig. 5A). Urine and feces were further collected at different timepoint and applied to investigate the silicon concentration in MB@MP and L-Arg@MP administration groups. Fig. 5K illustrated that the silicon concentration in the urine and feces of the rats gradually increased after the administration, reaching a peak at 24 h before dropping to the pre-administration level on the third day. This phenomenon suggested that these nano-drugs would be biodegraded under the stimulation of higher GSH, allowing the nano-drugs to be eliminated from the body. In addition, the liver was also the primary elimination route of nanocarriers. Collectively, these pharmacokinetics characteristics further indicated that the bioavailability of free drugs was significantly improved after being encapsulated into nanoparticle delivery system. Meanwhile, the prolonged blood half-life time will largely improving the delivery efficiency of drugs and the ultimate therapeutic effects.

3.9. *In vivo* anticancer effect of L-Arg/MB@MP

Encouraged by the potent PDT-GT synergistic effect *in vitro*, the therapeutic effect of L-Arg/MB@MP *in vivo* was further systematically investigated in MET-6 tumor-bearing BALB/c model mice. Detailed dosing regimens of different therapy groups and tumor monitoring processes were shown in Fig. 6A. During the whole therapeutic process, mice weights and tumor volumes were measured and record every 3 days following the experimental scheme. As depicted in Fig. 6B, the bodyweight of mice from the six treatment groups were stable throughout the entire therapeutic process, indicating excellent biosafety of therapeutic agents. In contrast, the mice weight decreased significantly in the control group (saline (+)) and nanocarriers alone group (MP(+)), which confirmed that the rapidly proliferating tumors could consume large amounts of nutrients resulting in weight loss. Meanwhile, the *in vivo* PDT-GT efficacy was evaluated by comparing tumor volume in tumor-bearing mice with different treatments (Fig. 6C). Specifically, mice treated with saline (+), MP(+), L-Arg, L-Arg@MP(+), and L-Arg/MB@MP failed to show an inhibitory effect on tumor growth. Mice injected with MB@MP(+) displayed a weak antitumor effect, further demonstrating insufficient oxygen supply did not completely exert the efficacy of PDT. Remarkably, tumors treated with L-Arg/MB@MP(+) were almost completely inhibited and the relative tumor volume (V/V_0) of that was 0.27 ± 0.11, indicating the significant synergistic effect of PDT and GT (Fig. 6E). The dramatic decrease in tumor weights after the treatments further confirmed the combined inhibitory effects of L-Arg/MB@MP(+) (Fig. 6D). In addition, a similar therapeutic tendency was also observed in the representative photos of tumor-bearing mice and isolated tumors (Figure S28 and **S29**).

In particular, a key feature of cancer cells is the loss of cell-cycle regulation, which will continuously stimulate cell proliferation and eventually tumors development [45]. Thus, the specific mechanism of L-Arg/MB@MP(+) inhibiting tumor growth was further explored by immunofluorescent staining and western blot assay. The fewer Ki67 positive signals (Fig. 6F) and more TUNEL positive signals (Fig. 6G) were observed in the L-Arg/MB@MP(+) group. Conversely, saline (+) and MP(+) groups showed distinctly tumor cell proliferation signaling. Additionally, the expression of apoptosis-related proteins of Bax, Bcl-2, and cleaved caspase-3 in mouse tumors following various therapies were also examined (Figure S30A). It was found that the amount of pro-apoptotic protein Bax in L-Arg/MB@MP(+) treated tumor tissues was almost 2-fold higher than that in control saline-treatment or MP-treated tumors (Figure S30B), while anti-apoptotic protein Bcl-2 showed the opposite trend (Figure S30C). And the presence of the cleaved caspase-3 in tumor cells indicated PDT-GT-induced proliferation inhibition and activation of apoptotic cell death (Figure S30D). Furthermore, the role of L-Arg/MB@MP(+) in inducing tumor cell apoptosis can be confirmed by the high secretion level of ATP (Figure S31) and HMGB1 (Figure S32) in the tumor tissues. The strong synergism of PDT and GT induced a significant secretion of ATP and HMGB1, which recruited DCs into the tumor sites to stimulate anti-tumor immunity. Therefore, the apparent inhibition of tumor cell proliferation and an enhanced apoptotic environment observed in PDT-GT-treated tumors likely contributed to enhance the immunotherapy in the mice.

Subsequently, the ability of L-Arg/MB@MP(+) in relieving tumor hypoxia and sensitizing PDT was further evaluated by a series of immunofluorescence staining. Tumor treated with saline (+) and MP(+) showed intense and dense green fluorescence, suggesting neovascularization, whereas the tumor region after intravenous injection with L-Arg/MB@MP(+) presented just faint green fluorescence (Fig. 7A). This indicated that the NO produced by GT can mediate the vasodilator activity to dilate blood vessels, and the ROS induced by PDT can kill tumor cells to inhibit angiogenesis. Meanwhile, neovascularization inhibition by L-Arg/MB@MP(+) will further promote relieving tumor hypoxia with high efficiency (Fig. 7B). As a virtuous circle, the effect of PDT will also be further amplified with more sufficient oxygen (Fig. 7C). Thus, these results similarly validate the assumption that L-Arg/MB@MP(+) relieves tumor inner hypoxia status to sensitize PDT, and finally realize an optimal synergistic therapeutic effect for tumor-bearing mice.

As L-Arg/MB@MP(+) mediated PDT-GT was highly immunogenic as above described, then the mechanism of immunotherapy was evaluated by collecting the tumors of mice after different treatments by immunofluorescence staining and FACS analysis. The percentages of $CD4^+$ and $CD8^+$ T cells among total $CD3^+$ cells significantly increased in the combination therapy in comparison with the saline group (Fig. 7D–F). Specifically, the percentage of both $CD4^+$ helper T lymphocytes and $CD8^+$ cytotoxic T cells greatly increased in L-Arg/MB@MP(+) group in comparison with the saline group (Figure S33A and **B**). It was obvious that percentages of $CD8^+$ cytotoxic T lymphocytes and $CD4^+$ helper T lymphocytes in the tumors clearly increased with time following L-Arg/MB@MP(+) treatment, indicating the ability of PDT-GT to drive effective T-cell infiltration into tumors. Most importantly, the results of H&E staining of main organs (Figure S34) and routine blood tests (Figure S35) indicated that the therapeutic groups did not cause acute toxicity to normal organs further proved L-Arg/MB@MP had good biocompatibility with potential in tumor treatment.

4. Conclusions

In summary, we successfully developed a GSH consumable and biodegradable drug delivery system by conjugating NO donor to photosensitizer for synergistic cancer PDT-GT therapy. In this nanosystem, ROS production could assist the conversion of L-Arg into NO and more toxic $ONOO^-$ to kill tumor cells directly and relieve tumor hypoxia, thus achieving more efficient tumor treatment than conventional PDT. The cell cycle arrest or apoptosis induced potent ICD along with the decreased expression of PDL-1 in cell surface can accelerate the immunosuppressive tumor microenvironment transformed into an immunostimulatory tumor microenvironment for enhanced systemic anti-tumor immunity. Moreover, MP carriers with disulfide-bonded configurations could prolong the circulation time and improve the bioavailability of free drugs resulting in enhancing the therapeutic activity. Taken together, such a well-defined L-Arg/MB@MP nanoplatform with great biodegradable and excellent therapeutic outcomes may provide a promising approach for PDT sensitization and anti-tumor immunotherapy.

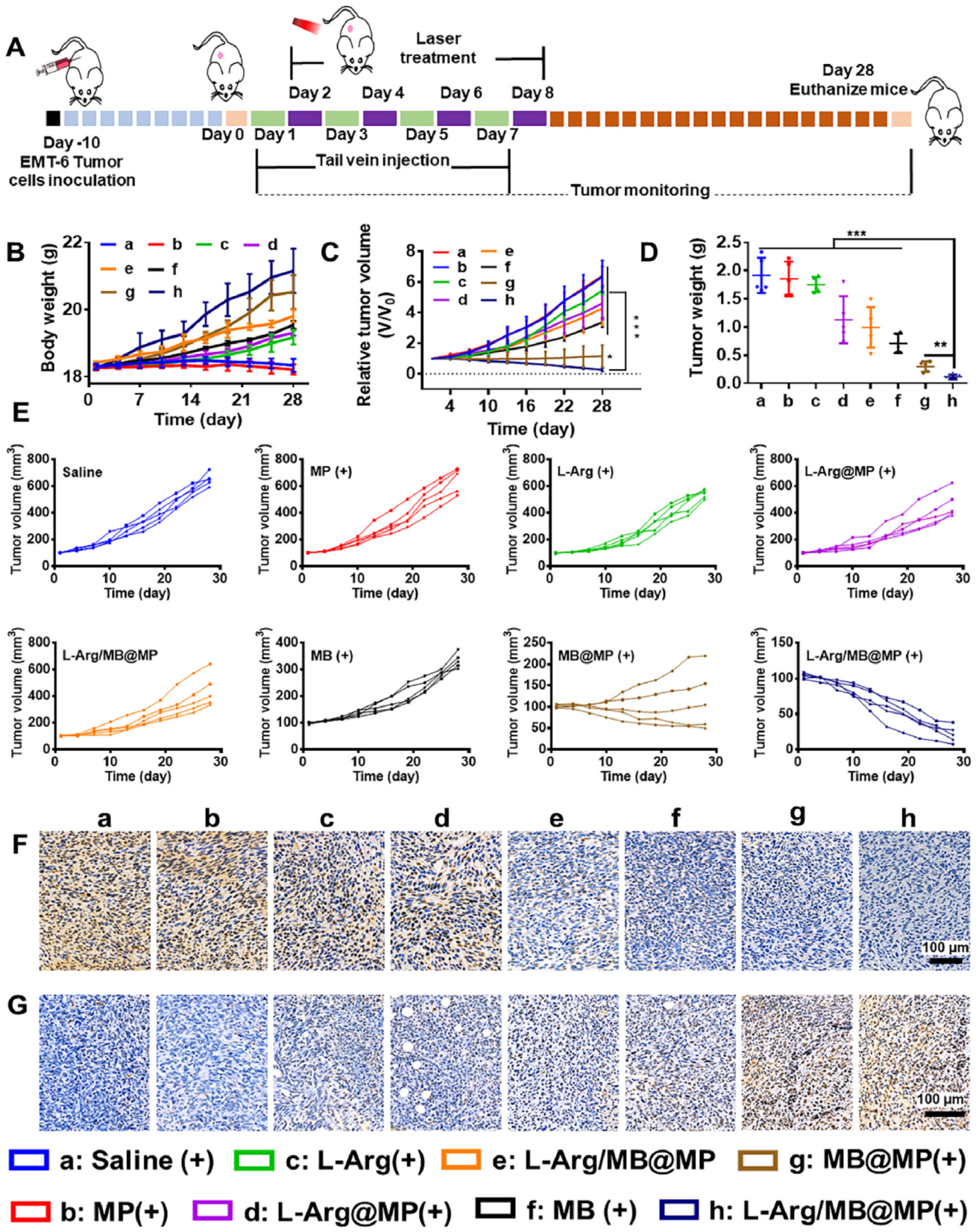

Fig. 6. Therapeutic effects of the nanosystem *in vivo*. (**A**) Schematic illustration of the *in vivo* therapeutic process. (**B**) Body weight curves of tumor-bearing mice in each group during the treatment. (**C**) Relative tumor volume in different therapeutics groups. (**D**) Average tumor weight after 28 days of various treatments. (**E**) Individual tumor growth kinetics in different groups during various treatments. Ki67 staining (**F**) and TUNEL staining (**G**) of tumor tissues with different groups on the 28th experimental day (scale bar = 100 μm). (+) represented laser irradiation (660 nm, 0.5 W/cm^2, 5 min). Data were shown the mean ± SD, n = 5. $^{**}p < 0.01$ and $^{***}p < 0.005$.

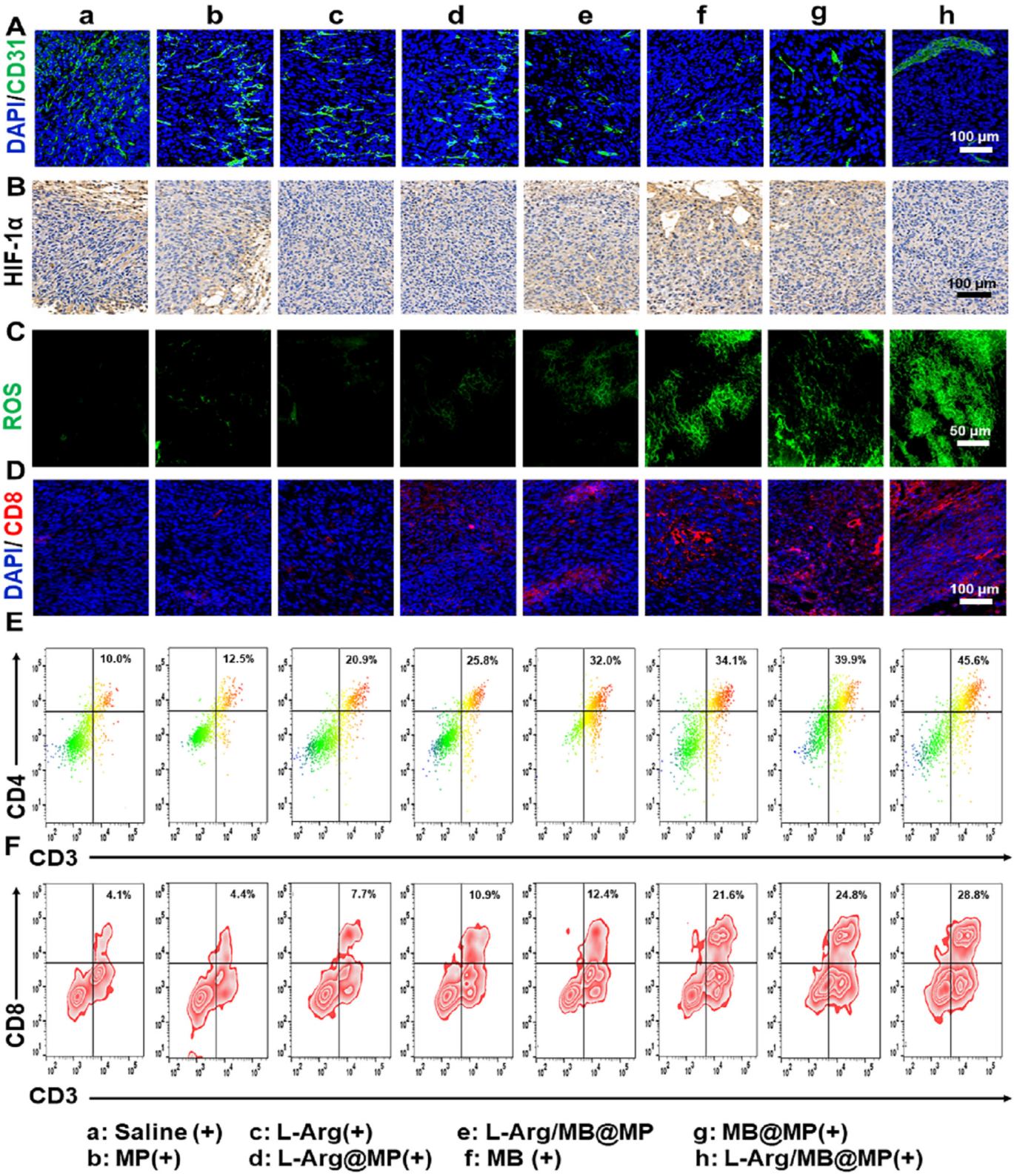

Fig. 7. *In vivo* antitumor study of EMT-6 tumor-bearing mice after different treatments. (**A**) Representative immunofluorescence staining images of CD31 in tumor sections after various treatments (scale bar = 100 μm). Green channel: CD31 positive cells; Blue channel: cell nuclei. (**B**) Representative immunohistochemistry staining images of HIF-1α in tumor sections after various treatments (scale bar = 100 μm). (**C**) Representative fluorescence images of ROS generation in tumor sections after various treatments (scale bar = 50 μm). (**D**) Representative immunofluorescence staining images of CD8 in tumor sections after various treatments (scale bar = 100 μm). Red channel: CD8 positive cells; Blue channel: cell nuclei. (**E**, **F**) Flow cytometric analysis of the intra-tumoral infiltration of CD4 and CD8 positive cytotoxic T lymphocyte. (+) represented laser irradiation (660 nm, 0.5 W/cm^2, 5 min).

Data availability

All data analyzed during this study are included in this published article (and its supplementary information files). Other raw data required to reproduce these findings are available from the corresponding author on reasonable request.

Credit author statement

Yi Feng, Hong Yang, and Yiyao Liu conceived the study, analyzed the data, and drafted the manuscript. Tingting Li, Xiang Qin, Shun Li, Fengming You, and Chunhui Wu critically revised the manuscript for important intellectual content. Hanxi Zhang, Xiaoxue Xie, Yu Chen, Xiaodan Wei, Geng Yang, Ningxi Li, and Mengyue Li assisted in data collection and study design. All authors read and approved the final manuscript.

Declaration of competing interest

The authors declare that they have no known competing financial interests or personal relationships that could have appeared to influence the work reported in this paper.

Acknowledgments

This research was supported, in part or in whole, by the National Natural Science Foundation of China (U19A2006, 12132004, 11972111, 31900940, 32071304, 32171309, 32171395), the Sichuan Science and Technology Program (21YJ0130), and the Joint Funds of Center for Engineering Medicine (ZYGX2021YGLH017, ZYGX2021YGLH010, ZYGX2021YGLH023).

Appendix A. Supplementary data

Supplementary data to this article can be found online at https://doi.org/10.1016/j.mtbio.2022.100288.

References

[1] L. Zhang, Y. Li, W. Che, et al., AIE multinuclear Ir(III) complexes for biocompatible organic nanoparticles with highly enhanced photodynamic performance, Adv. Sci. 6 (2019) 1802050.
[2] G. Deng, Z. Sun, S. Li, et al., Cell-membrane immunotherapy based on natural killer cell membrane coated nanoparticles for the effective inhibition of primary and abscopal tumor growth, ACS Nano 12 (2018) 12096–12108.
[3] D. Xi, N. Xu, X. Xia, et al., Strong π–π stacking stabilized nanophotosensitizers: improving tumor retention for enhanced therapy for large tumors in mice, Adv. Mater. 34 (2022) 2106797.
[4] L. Hu, P. Wang, M. Zhao, et al., Near-infrared rechargeable "optical battery" implant for irradiation-free photodynamic therapy, Biomaterials 163 (2018) 154–162.
[5] S. Fu, R. Yang, L. Zhang, et al., Biomimetic CoO@AuPt nanozyme responsive to multiple tumor microenvironmental clues for augmenting chemodynamic therapy, Biomaterials 257 (2020) 120279.
[6] L. Cheng, A. Kamkaew, H. Sun, et al., Dual-modality positron emission tomography/optical image-guided photodynamic cancer therapy with chlorine6-containing nanomicelles, ACS Nano 10 (2016) 7721–7730.
[7] S. Phua, G. Yang, W.Q. Lim, et al., Catalase-integrated hyaluronic acid as nanocarriers for enhanced photodynamic therapy in solid tumor, ACS Nano 13 (2019) 4742–4751.
[8] L.Y. Chen, L. Wang, Y.X. Ren, et al., The circular RNA circ-ERBIN promotes growth and metastasis of colorectal cancer by miR-125a-5p and miR-138-5p/4EBP-1 mediated cap-independent HIF-1alpha translation, Mol. Cancer 19 (2020) 164.
[9] S.I. Grivennikov, F.R. Greten, M. Karin, Immunity, inflammation, and cancer, Cell 140 (2010) 883–899.
[10] M. Mazzone, D. Dettori, R.L. de Oliveira, et al., Heterozygous deficiency of PHD2 restores tumor oxygenation and inhibits metastasis via endothelial normalization, Cell 136 (2009) 839–851.
[11] Y. Yang, W. Zhu, L. Feng, et al., G-quadruplex-based nanoscale coordination polymers to modulate tumor hypoxia and achieve nuclear-targeted drug delivery for enhanced photodynamic therapy, Nano Lett. 18 (2018) 6867–6875.
[12] D. Zhang, M. Wu, Z. Cai, et al., Chemotherapeutic drug based metal-organic particles for microvesicle-mediated deep penetration and programmable pH/NIR/hypoxia activated cancer photochemotherapy, Adv. Sci. 5 (2018) 1700648.
[13] Y. Dai, C. Xu, X. Sun, et al., Nanoparticle design strategies for enhanced anticancer therapy by exploiting the tumour microenvironment, Chem. Soc. Rev. 46 (2017) 3830–3852.
[14] L. Kalafati, I. Kourtzelis, J. Schulte-Schrepping, et al., Innate immune training of granulopoiesis promotes anti-tumor activity, Cell 183 (2020) 771–785.
[15] J. An, Y.G. Hu, C. Li, et al., A pH/Ultrasound dual-response biomimetic nanoplatform for nitric oxide gas-sonodynamic combined therapy and repeated ultrasound for relieving hypoxia, Biomaterials 230 (2020) 119636.
[16] S.S. Wan, J.Y. Zeng, H. Cheng, et al., ROS-induced NO generation for gas therapy and sensitizing photodynamic therapy of tumor, Biomaterials 185 (2018) 51–62.
[17] D.W. Zheng, B. Li, C.X. Li, , et al.X.Z. Zhang, Photocatalyzing CO2 to CO for enhanced cancer therapy, Adv. Mater. 29 (44) (2017).
[18] S. Li, R. Liu, X. Jiang, et al., Near-infrared light-triggered sulfur dioxide gas therapy of cancer, ACS Nano 13 (2019) 2103–2113.
[19] P. Gao, H. Wang, Y.Y. Cheng, Strategies for efficient photothermal therapy at mild temperatures: progresses and challenges, Chin. Chem. Lett. 33 (2022) 575–586.
[20] Y. Sun, S. Chen, X. Chen, et al., A highly selective and recyclable NO-responsive nanochannel based on a spiroring opening-closing reaction strategy, Nat. Commun. 10 (2019) 1323.
[21] Z. Hou, Y. Wu, C. Xu, et al., Precisely structured nitric-oxide-releasing copolymer brush defeats broad-spectrum catheter-associated biofilm infections in vivo, ACS Cent. Sci. 6 (2020) 2031–2045.
[22] Q. Shao, B. Xing, Photoactive molecules for applications in molecular imaging and cell biology, Chem. Soc. Rev. 39 (2010) 2835–2846.
[23] M.M. Wan, H. Chen, W.Z. Da, et al., Nitric oxide-driven nanomotor for deep tissue penetration and multidrug resistance reversal in cancer therapy, Adv. Sci. 8 (2021) 2002525.
[24] R.K. Kim, Y. Suh, Y.H. Cui, et al., Fractionated radiation-induced nitric oxide promotes expansion of glioma stem-like cells, Cancer Sci. 104 (2013) 1172–1177.
[25] X. Zhang, J. Du, Z. Guo, et al., Efficient near infrared light triggered nitric oxide release nanocomposites for sensitizing mild photothermal therapy, Adv. Sci. 6 (2019) 1801122.
[26] Y. Deng, F. Jia, S. Chen, et al., Nitric oxide as an all-rounder for enhanced photodynamic therapy: hypoxia relief, glutathione depletion and reactive nitrogen species generation, Biomaterials 187 (2018) 55–65.
[27] J.P. Pinto, S. Ribeiro, H. Pontes, et al., Erythropoietin mediates hepcidin expression in hepatocytes through EPOR signaling and regulation of C/EBPalpha, Blood 111 (2008) 5727–5733.
[28] J.J. Lancaster, A tutorial on the diffusibility and reactivity of free nitric oxide, Nitric Oxide 1 (1997) 18–30.
[29] M.S. Hadipour, M. Yazdimamaghani, H. Ghandehari, Glutathione-sensitive hollow mesoporous silica nanoparticles for controlled drug delivery, J. Contr. Release 282 (2018) 62–75.
[30] P. Huang, Y. Chen, H. Lin, et al., Molecularly organic/inorganic hybrid hollow mesoporous organosilica nanocapsules with tumor-specific biodegradability and enhanced chemotherapeutic functionality, Biomaterials 125 (2017) 23–37.
[31] W. Chen, P. Zhong, F. Meng, et al., Redox and pH-responsive degradable micelles for dually activated intracellular anticancer drug release, J. Contr. Release 169 (2013) 171–179.
[32] L. Yu, Y. Chen, H. Lin, et al., Ultrasmall mesoporous organosilica nanoparticles: morphology modulations and redox-responsive biodegradability for tumor-specific drug delivery, Biomaterials 161 (2018) 292–305.
[33] L. Sun, D. Wang, Y. Chen, et al., Core-shell hierarchical mesostructured silica nanoparticles for gene/chemo-synergetic stepwise therapy of multidrug-resistant cancer, Biomaterials 133 (2017) 219–228.
[34] M. Wu, Q. Meng, Y. Chen, et al., Large-pore ultrasmall mesoporous organosilica nanoparticles: micelle/precursor co-templating assembly and nuclear-targeted gene delivery, Adv. Mater. 27 (2015) 215–222.
[35] G. Saito, J.A. Swanson, K.D. Lee, Drug delivery strategy utilizing conjugation via reversible disulfide linkages: role and site of cellular reducing activities, Adv. Drug Deliv. Rev. 55 (2003) 199–215.
[36] Y. Feng, X. Xie, H. Zhang, et al., Multistage-responsive nanovehicle to improve tumor penetration for dual-modality imaging-guided photodynamic-immunotherapy, Biomaterials 275 (2021) 120990.
[37] S. Piletsky, F. Canfarotta, A. Poma, et al., Molecularly imprinted polymers for cell recognition, Trends Biotechnol. 38 (2020) 368–387.
[38] X. He, X. Wu, K. Wang, et al., Methylene blue-encapsulated phosphonate-terminated silica nanoparticles for simultaneous in vivo imaging and photodynamic therapy, Biomaterials 30 (2009) 5601–5609.
[39] S.H. Seo, B.M. Kim, A. Joe, et al., NIR-light-induced surface-enhanced Raman scattering for detection and photothermal/photodynamic therapy of cancer cells using methylene blue-embedded gold nanorod@SiO2 nanocomposites, Biomaterials 35 (2014) 3309–3318.
[40] J. Chen, L. Keltner, J. Christophersen, et al., New technology for deep light distribution in tissue for phototherapy, Cancer J. 8 (2002) 154–163.
[41] X. Cheng, S. Zhang, H. Liu, et al., Biomimetic metal-organic framework composite-mediated cascade catalysis for synergistic bacteria killing, ACS Appl. Mater. Interfaces 12 (2020) 36996–37005.
[42] S.K. Natarajan, S. Venneti, Glutamine metabolism in brain tumors, Cancers 11 (2019).
[43] M.V. Yezhelyev, L. Qi, R.M. O'Regan, S. Nie, et al., Proton-sponge coated quantum dots for siRNA delivery and intracellular imaging, J. Am. Chem. Soc. 130 (2008) 9006–9012.
[44] J. Shan, X. Li, K. Yang, et al., Efficient bacteria killing by Cu2WS4 nanocrystals with enzyme-like properties and bacteria-binding ability, ACS Nano 13 (2019) 13797–13808.

[45] Y. Shi, X. Ding, Z.H. He, et al., Critical role of TRPC6 channels in G2 phase transition and the development of human oesophageal cancer, Gut 58 (2009) 1443–1450.
[46] J. Liu, H. Liang, M. Li, et al., Tumor acidity activating multifunctional nanoplatform for NIR-mediated multiple enhanced photodynamic and photothermal tumor therapy, Biomaterials 157 (2018) 107–124.
[47] C. Zhang, Z. Zeng, D. Cui, et al., Semiconducting polymer nano-PROTACs for activatable photo-immunometabolic cancer therapy, Nat. Commun. 12 (2021) 2934.
[48] X. Zhao, K. Zhang, Y. Wang, et al., Intracellular self-assembly driven nucleus-targeted photo-immune stimulator with chromatin decompaction function for robust Innate and adaptive antitumor immunity, Adv. Funct. Mater. 32 (2022) 2108883.
[49] Y. Fuchs, H. Steller, Programmed cell death in animal development and disease, Cell 147 (2011) 742–758.
[50] M. Yu, X. Duan, Y. Cai, et al., Multifunctional nanoregulator reshapes immune microenvironment and enhances immune memory for tumor immunotherapy, Adv. Sci. 6 (2019) 1900037.
[51] R. Vogel, Listening to the endothelium: a story of signal and noise, J. Am. Coll. Cardiol. 51 (2008) 1965–1966.
[52] W.-H. An, M. Mamuti, X. Wang, et al., Rationally designed modular drug delivery platform based on intracellular peptide self-assembly, Exploration 1 (2021) 20210153.